

MULTI-PHASE HIGH-VELOCITY CLOUDS TOWARD HE 0226–4110 AND PG 0953+414¹

ANDREW J. FOX², BART P. WAKKER, & BLAIR D. SAVAGE,
Department of Astronomy, University of Wisconsin - Madison, 475 North Charter St., Madison, WI 53706

TODD M. TRIPP,
Department of Astronomy, University of Massachusetts, 640 Lederle Graduate Research Center, Amherst, MA 01003

KENNETH R. SEMBACH,
Space Telescope Science Institute, 3700 San Martin Drive, Baltimore, MD 21218

AND

JOSS BLAND-HAWTHORN
Anglo-Australian Observatory, PO Box 296, Epping, NSW 2121, Australia
Draft version January 1, 2018

ABSTRACT

We study the physical conditions, elemental abundances, and kinematics of the high-velocity clouds (HVCs) along the sight lines toward active galaxies HE 0226–4110 and PG 0953+414 using *Hubble Space Telescope Imaging Spectrograph* and *Far Ultraviolet Spectroscopic Explorer* data. No 21-cm H I emission is detected in these clouds, but our observations reveal multiple components of HVC absorption in lines of H I, C II, C III, C IV, O VI, Si II, Si III, and Si IV in both directions. We investigate whether photoionization by the extragalactic background radiation or by escaping Milky Way radiation can explain the observed ionization pattern. We find that photoionization is a good explanation for the C II, C III, Si II, and Si III features, but not for the O VI or C IV associated with the HVCs, suggesting that two principal phases exist: a warm ($T \approx 10^4$ K), photoionized phase and a hotter ($T = 1 - 3 \times 10^5$ K), collisionally-ionized phase; the broader line widths of the high ions are consistent with this multi-phase hypothesis. The warm HVCs toward HE 0226–4110 have high levels of ionization (97–99%), and metallicities ($[Z/H]$ between -0.9 and -0.4) close to those in the Magellanic Stream, which lies eleven degrees away on the sky at similar velocities. These HVCs may well be stripped fragments of the Stream that have been ionized by the pervading radiation field; they have thermal pressures that would place them close to equilibrium in a fully ionized 10^6 K Galactic corona with $n_H = 4 - 9 \times 10^{-5} \text{ cm}^{-3}$ at 50 kpc. The warm HVCs seen at -146 and 125 km s^{-1} toward PG 0953+414 have $[Z/H] = -0.6 \pm 0.2$ and -0.8 ± 0.2 , respectively, suggesting they are not formed from purely Galactic material. A mini-survey of the hot, collisionally ionized HVC components seen here and in five other sight lines finds that in 11/12 cases, the high ions have kinematics and ionic ratios that are consistent with an origin in conductive interfaces, where energy flows into the HVCs from a hot surrounding medium and produces O VI and C IV-bearing boundary layers. However, the broad absorption wing on the O VI profile toward PG 0953+414 is *not* completely explained by the interface scenario. This feature may be tracing the outflow of hot gas into the Milky Way halo as part of a Galactic fountain or wind.

Subject headings: Galaxy: halo – intergalactic medium – ISM: clouds – ultraviolet: ISM

1. INTRODUCTION

Surrounding the Milky Way galaxy lies a population of diffuse gaseous clouds that are not co-rotating with the disk. First discovered in 21-cm emission by Muller, Oort, & Raimond (1963), no single model has been able to simultaneously explain the kinematics, metallicity, and emission properties of these so-called high-velocity clouds (HVCs) (Wakker & van Woerden 1997). The failure to find HVCs distributed throughout

other galaxy groups (Pisano et al. 2004) together with HVC detections around M31 (Braun & Thilker 2004) suggest that HVCs are typically associated with large galaxies, rather than the Local Group. Within this paradigm, many HVCs (e.g., Complex C, Wakker et al. 1999) could represent material leftover from the galaxy formation process (Oort 1970; Maller & Bullock 2004), or else material stripped from nearby galaxies (e.g., the Magellanic Stream, Gardiner & Noguchi 1996). Studying and understanding HVCs allows us to trace the interactions and feedback between galaxies and the intergalactic medium. HVCs regulate the rate of star formation in our own Galaxy, by providing gaseous material from which new stars are born.

A new phase of gas in HVCs was discovered with the detections of high-velocity C IV (Sembach et al. 1995, 1999) and O VI absorption (Sembach et al. 2000;

¹ Based on observations from the NASA-CNES-CSA *Far Ultraviolet Spectroscopic Explorer* mission, operated by Johns Hopkins University, supported by NASA contract NAS 5-32985, and from the NASA/ESA *Hubble Space Telescope*, obtained at the Space Telescope Science Institute, which is operated by the Association of Universities for Research in Astronomy, Inc., under NASA contract NAS 5-26555.

² E-mail fox@astro.wisc.edu

Murphy et al. 2000). A recent survey of extragalactic sight lines with the *Far Ultraviolet Spectroscopic Explorer* (*FUSE*) satellite (Sembach et al. 2003, hereafter S03) has found that high-velocity O VI absorption is detected at $>3\sigma$ significance 84 times in a survey of 102 sight lines. Many of these high-velocity O VI features are spatially and kinematically associated with known 21-cm emitting H I structures, for example Complex C, Complex A, and the Magellanic Stream (S03, Fox et al. 2004). There are other cases where O VI HVCs have no counterparts detected in H I 21-cm emission. However, studies of such highly ionized HVCs (Collins et al. 2004, 2005; Ganguly et al. 2005) have found absorption in the H I Lyman series and in other metal-line tracers of neutral and weakly ionized gas at the same velocities as the high ions. The high ion-low ion connections in HVCs are well explained by an arrangement where the hot gas arises in the boundary layers between the neutral HVC and the surrounding medium (Fox et al. 2004).

A separate class of high-velocity O VI absorber exists in the form of broad, shallow absorption wings at positive velocities. Unlike many of the discrete high velocity O VI absorption features seen along complete paths through the Galactic halo and corona, the O VI positive-velocity wings manifest themselves as continuous absorption troughs extending from velocities indicative of Galactic halo gas ($|v_{LSR}| < 100 \text{ km s}^{-1}$) out to velocities of several hundred km s^{-1} . A majority of positive-velocity wings (17/21) are found in the Northern Galactic hemisphere, at $l=180\text{--}300^\circ$ and $b > 30^\circ$, even though the sample of sight lines is spread fairly evenly around the sky (S03). Such a trend may be related to the general enhancement of O VI in the Northern hemisphere of the Galactic halo (Savage et al. 2003), and to the opening of the Local Bubble in this direction (Welsh et al. 1999).

In this paper we present high-resolution Space Telescope Imaging Spectrograph (STIS) observations complemented with *FUSE* data to explore the high-velocity absorption in one direction showing high-velocity O VI components (HE 0226–4110) and one showing a high-velocity O VI wing (PG 0953+414). Basic properties of the two sight lines under study are found in Table 1.

The line of sight to Seyfert 1 galaxy HE 0226–4110 ($l = 253.94^\circ$, $b = -65.78^\circ$, $z_{em} = 0.495$) lies 10.8° from the $N(\text{H I}) = 2.0 \times 10^{18} \text{ cm}^{-2}$ (5σ) contour of H I 21-cm emission from the Magellanic Stream (Figure 1, left panel). The Magellanic Stream is a broad filament of material covering ~ 1000 square degrees in an arc extending from $l \approx 90^\circ$, $b \approx -45^\circ$, through the South Galactic pole and around to positive latitudes (Putman et al. 2003a; Brüns et al. 2005). The Stream is believed to be gas stripped out of the Magellanic Clouds by tidal forces as the Clouds orbit the Milky Way (Gardiner & Noguchi 1996). Six sight lines passing through the Magellanic Stream have O VI detections at similar velocities to the H I (Figure 15 in S03), suggesting that the Stream contains (or is surrounded by) a highly ionized component.

PG 0953+414 is a Seyfert 1 galaxy at $z_{em} = 0.239$ lying at $l=179.79^\circ$, $b=+51.71^\circ$. Various nearby H I structures can be seen in Figure 1 (right panel). This direction has the advantage of being very close the anticenter direction ($l=180^\circ$), perpendicular to the direction of LSR motion, so the effects of Galactic rotation on absorption line profiles are removed. PG 0953+414 is therefore ide-

ally situated for use as a backlight to study the inflow and outflow of gaseous material.

The structure of this paper is as follows. In §2 we describe the observations and data reduction. In §3 our spectroscopic measurement and analysis techniques are discussed. In §4 and §5 we discuss our observations of the high-velocity absorption systems seen toward HE 0226–4110 and PG 0953+414, respectively. We discuss photoionization modeling of the HVCs in §6, and collisional ionization modeling of the highly ionized species in §7. Section 8 is devoted to understanding the origin of the O VI wing absorption seen toward PG 0953+414. The principal results of our study are summarized in §9.

2. OBSERVATIONS AND DATA REDUCTION

HE 0226–4110 and PG 0953+414 were each observed on several occasions with the E140M echelle mode of the STIS instrument (Woodgate et al. 1998; Kimble et al. 1998), which provides spectra at 7 km s^{-1} resolution (FWHM) in the range 1150–1700 Å, with a few small gaps between orders at $\lambda > 1600 \text{ Å}$. Details of these observations are given in Table 2. The data were reduced as described in Tripp et al. (2001) including the two-dimensional scattered light correction developed by the STIS Instrument Definition Team (Landsman & Bowers 1997; Bowers et al. 1998). In general, the wavelength calibration of STIS data is excellent; Kim Quijano et al. (2003) report that the relative wavelength calibration is accurate to 0.25–0.5 pixels across the entire spectrum, and the absolute wavelength calibration is accurate to ~ 1 pixel (3.2 km s^{-1}). The overall velocity uncertainty in our data was verified by cross-checking the centers of Galactic metal-line absorption in O I $\lambda 1302.169$, Fe II $\lambda 1608.451$, Si II $\lambda 1304.370$, Si II $\lambda 1526.707$, Ni II $\lambda 1317.217$, S II $\lambda 1253.811$, and S II $\lambda 1250.584$.

The *FUSE* satellite (Moos et al. 2000; Sahnou et al. 2000) provided the far-UV spectra of HE 0226–4110 and PG 0953+414 (Table 2). For wavelengths below 1000 Å, we use data from the SiC2A detector segment only. We did not combine with data from the SiC1B detector segment data because this detector has lower sensitivity and resolution. For wavelengths between 1000 and 1187 Å, we use coadded LiF1 and LiF2 data, since the resolution difference between these two channels is small. The data were reduced with the data reduction pipeline CALFUSE (v2.1.6 or v2.4.0). Even after the application of the pipeline, velocity shifts have to be determined for each exposure and each detector segment before coaddition of the spectra to obtain accurate wavelength solutions (see §3.4 in Wakker et al. 2003). We measured the average velocity centroid of all the unsaturated neutral ISM lines clearly detected in each *FUSE* segment (Si II $\lambda 1020.699$, Ar I $\lambda 1048.220$, N I $\lambda 1134.165$, 1134.415 , 1134.980 , and numerous H₂, Fe II, and O I lines), and then determined the offset from the centers of neutral ISM lines seen in the STIS data. This “bootstrapping” technique allows the kinematics of absorption line profiles observed with *FUSE* and STIS to be reliably compared. All velocities quoted in this paper are referenced to the Local Standard of Rest (LSR). Note that no velocity difference was found between the metal lines and the H₂ lines. The offsets for the LiF channels are typically $\approx 10 \text{ km s}^{-1}$ but in the SiC channels they can be as high as $\approx 40 \text{ km s}^{-1}$. We estimate a residual 1σ zero-point error of 5 km s^{-1}

after this process has been applied, since 5 km s^{-1} is the dispersion of post-correction velocity centroid measurements of neutral lines in the *FUSE* data. This velocity error is propagated in calculating the systematic errors on our absorption line measurements.

Continua were fitted to both the *FUSE* and STIS data in regions approximately 1000 km s^{-1} wide around each absorption line of interest, using regions of the spectra judged to be free from absorption. In almost all cases a linear continuum could be fitted, since our target active galaxies have flat UV spectra generated by non-thermal emission processes.

All *FUSE* data were rebinned by five pixels to provide optimal sampling, for both display and measurement. The raw STIS spectra are already optimally sampled, so we measure the absorption using the unbinned data, but since the STIS spectra for both HE 0226–4110 and PG 0953+414 are very noisy, we use 2-pixel rebinning for display³.

For each of our two studied sight lines we display H I 21-cm emission spectra, to emphasize the low $N(\text{H I})$ of the highly ionized HVCs under study. For the HE 0226–4110 direction these data were obtained and provided by R. Morras, using the Villa Elisa telescope, which has a beam size of $34'$; some residual uncertainty in the baseline fit is present in the range $\pm 100 \text{ km s}^{-1}$. For PG 0953+414, we use spectra from the Effelsberg telescope (Wakker et al. 2001) with a $9'.7$ beam. Both data sets have an approximate velocity resolution of 1 km s^{-1} , and have been corrected for side lobe contamination.

3. SPECTROSCOPIC MEASUREMENTS

We identified the high-velocity component structure in each sight line using the high-resolution STIS observations of metal-line absorption, particularly in the C II $\lambda 1334.532$, Si II $\lambda 1260.422$, Si II $\lambda 1193.290$, and Si III $\lambda 1206.500$ lines. We then estimated the velocity range covered by each absorption component, and measured the equivalent width of the absorption between these limits in all spectral lines present in the data. We converted the measured optical depth in the line as a function of velocity into apparent column densities, $N_a(v)$, using the relation $N_a(v) = 3.768 \times 10^{14} (f\lambda)^{-1} \tau_a(v)$ ions $\text{cm}^{-2} (\text{km s}^{-1})^{-1}$, where the apparent optical depth (AOD) is given by $\tau_a(v) = \ln[F_c(v)/F(v)]$, f is the oscillator strength of the transition (taken from Morton 2003), λ is the transition wavelength in Angstroms, and $F(v)$ and $F_c(v)$ are the observed line and continuum fluxes at velocity v , respectively (Savage & Sembach 1991). Integrating $N_a(v)$ between two chosen velocity limits determines the total column density in that velocity range, and the optical depth-weighted average values of v and $\sqrt{(v - \bar{v})^2}$, i.e. the first and second moments of $\tau_a(v)$, give measurements of the line center and line width (Sembach & Savage 1992).

The AOD technique requires no prior knowledge of the component structure. It will produce good results as long as the line profiles are resolved and not saturated. STIS/E140M, *FUSE*/LiF, and *FUSE*/SiC can resolve lines with $b > 4, 12,$ and 15 km s^{-1} , respectively.

³ Exception: in one case, where we need the highest possible resolution to emphasize the component structure, we show the fully sampled spectra (§4.3).

Wakker et al. (2003) show a comparison of the apparent column density of O VI from both members of the doublet toward HE 0226–4110 and PG 0953+414 in the velocity range -400 to 400 km s^{-1} ; this data shows that no unresolved saturation affects the zero-velocity (Milky Way disk and halo) O VI absorption. By inference, the weaker high-velocity O VI absorption, of interest here, is also likely to be unsaturated. The O VI lines are likely to be resolved since the high temperatures of the regions where O VI is found result in lines with thermal widths $b > 18 \text{ km s}^{-1}$. However, *FUSE* absorption line profiles of the H I Lyman lines may be unresolved, making saturation hard to detect. As one measures progressively weaker Lyman series absorption lines, the f -values of the transitions decrease, and eventually the lines will become unsaturated. At this point, consecutive Lyman lines will give the same value for N_a ; this occurred for the HVCs along our two sight lines with the H I $\lambda 920.963, 919.351, 918.129,$ and 917.181 lines. To check the column densities derived from AOD integrations of these lines, we construct a Voigt profile model and compare with the data. For the low-velocity components, we take the parameters from the fits to the 21-cm profiles in our two target directions (Wakker et al. 2003); for the high-velocity components, we take the velocities, widths, and column densities defined by the AOD integrations. All components are convolved with a Gaussian line spread function (with FWHM 25 km s^{-1} for the *FUSE*/SiC channels). Our model also reproduces the D I and O I lines when $D/H = 2 \times 10^{-5}$ and O/H is solar, assuming they have the same width as the H I lines (i.e., non-thermal broadening dominates). Small adjustments ($\approx 5 \text{ km s}^{-1}$) are needed to the *widths* of each H I component to produce a good fit⁴, but the AOD *column densities* reproduce the depth of absorption well. We thus have confidence in the values of $N(\text{H I})$ derived from the AOD method. A full Voigt profile *fit* of the H I Lyman series absorption lines, involving minimizing χ^2 for a grid of different values of $\log N(\text{H I})$ and $b(\text{H I})$, was attempted, but did not produce reliable results given the overlapping component structure, poor S/N, numerous blends, and degeneracy between N and b .

To check for the possibility of saturation in the strong metal lines (C II, C III, Si II, Si III), Voigt profile models were constructed in the same manner as for the H I lines (using the column densities from the $N_a(v)$ integrations) and compared with the observations. We investigated how saturated the observed profiles could be by increasing the model component column densities and noting whether the quality of the fit decreases. For the cases of the C III and Si III lines toward HE 0226–4110, saturation is clearly possible in some HVC components, resulting in large positive errors (as large as 1 dex) in $\log N$.

⁴ For PG 0953+414, we found that in addition to the HVCs measured here, two extra components were needed to reproduce the Lyman series and O I absorption line profiles. A component at -110 km s^{-1} , with $N(\text{H I}) = 1 - 2 \times 10^{17}$ is needed. This component is also seen in the negative-velocity wings of Si II $\lambda 1260.422$ and Si III $\lambda 1206.500$, and in H I 21-cm emission at this velocity less than 2° away, in HVC MIII (see Figure 1). A second component at $+55 \text{ km s}^{-1}$ with $N(\text{H I}) = 1 - 2 \times 10^{17} \text{ cm}^{-2}$ is needed to fill in the H I absorption between the zero-velocity component and the positive-velocity HVC. Neither of these components changes the H I column density of the HVCs under study in this paper.

The full absorption line measurements are presented on a component-by-component basis for the HE 0226–4110 system in Table 3, and for the PG 0953+414 system in Table 4. We list the component velocity, width, and column density measurements returned by the AOD method, the equivalent width, and the observed S/N near the line, measured per resolution element in the continuum. When no absorption is detected in a particular feature, we calculate a 3σ upper limit for the ionic column density using the error on the equivalent width measurement, converted to a column density limit assuming a linear curve-of-growth⁵.

Two sets of errors are quoted for each measurement of equivalent width and column density. The first is a quadrature sum of statistical uncertainty in the count rate (Poisson noise) and the continuum placement uncertainty. The second is the systematic error, found from a quadrature addition of fixed pattern noise (f.p.n.) in the detectors with the velocity scale errors. We estimated the f.p.n. per unbinned pixel to be 1% for STIS detectors, 2.5% for *FUSE* observations of HE 0226–4110, and 10% for *FUSE* observations of PG 0953+414. The f.p.n. is lower in the HE 0226–4110 *FUSE* dataset due to the use of focal-plane (FP) splits for some observations, which place the spectra in different positions on the detector. These errors imply that any feature weaker than 1.8 mÅ (6.3 mÅ) could be caused by f.p.n. in the HE 0226–4110 (PG 0953+414) *FUSE* data. The velocity error ($\pm 5 \text{ km s}^{-1}$) allows for the intrinsic uncertainty in the zero point of the post-calibration velocity scale, and the uncertainty in the choice of velocities used to define a particular high-velocity component. The latter uncertainty is important since the different components of high-velocity absorption are not always distinct from each other and placing the division can be difficult. We calculate the effect of this error by changing the velocity extrema of each component by $\pm 5 \text{ km s}^{-1}$ and observing the change in the equivalent width and in N_a .

For each sight line we have prepared three plots showing the absorption line data (Figures 2, 3, and 4 for HE 0226–4110 and Figures 5, 6, and 7 for PG 0953+414). First we display (Figs. 2 and 5) the fully-reduced spectra for all absorption lines in which high-velocity absorption is detected, using gray shading to identify the gas in the high-velocity components. We also include H I 21-cm emission line spectra of our two sight lines in the upper left panels. In Figures 3 and 6 we include stacks of H I Lyman series absorption profiles. These figures show the presence of high-velocity H I absorption in the Lyman series from $\text{Ly}\gamma$ at 972.537 \AA ($n = 1 \rightarrow 4$) down to $\text{Ly}\mu$ at 917.181 \AA ($n = 1 \rightarrow 13$). At wavelengths shortward of $\text{Ly}\mu$ the flux goes to zero. $\text{Ly}\alpha$ is too broad and $\text{Ly}\beta$ is too polluted by geocoronal emission (O I airglow) to show the high-velocity component structure. Geocoronal emission in the stronger Lyman lines tends to “fill in” absorption in the approximate range -100 to 100 km s^{-1} , so we display night-only data for the H I lines to minimize this effect; at high velocities the geocoronal emission becomes insignificant. Our final method of displaying the data is to compare the apparent column density profiles of particular lines (Figures 4 and 7).

⁵ The relation used is $N = 1.13 \times 10^{17} W_\lambda / \lambda^2 f$, where N is in cm^{-2} , W_λ is the 3σ equivalent width limit in mÅ, and λ is in Å.

3.1. Blends toward HE 0226–4110

An IGM absorption line system at $z = 0.34028$ is seen in $\text{Ly}\alpha$, $\text{Ly}\beta$, C III, O IV, and O VI (Lehner et al. 2005). Absorption at this redshift by Ne VIII $\lambda 770.409$ would blend with high-velocity absorption from the strong line of O VI at 1031.926 \AA in the range $150\text{--}210 \text{ km s}^{-1}$. We used the redshifted absorption data for the weak line in the Ne VIII doublet ($\lambda 780.324$) to assess the strength of the blend; the weak line shows no absorption at the same redshift, with $W_\lambda(\text{Ne VIII}) < 9 \text{ m\AA}$ (3σ) integrated over 60 km s^{-1} (the width of the O VI lines in the IGM system). Therefore the strength of the Ne VIII $\lambda 770.409$ blend must be $< 18 \text{ m\AA}$ (3σ), since $f_{770}/f_{780} = 2$. The total absorption in the range $160\text{--}230 \text{ km s}^{-1}$ in the frame of the O VI line has $W_\lambda = 45 \pm 5 \pm 5 \text{ m\AA}$, more than can be accounted for by the blend, so we proceed by treating this as a true detection of O VI.

Absorption from the $J = 4$ rotational level of molecular hydrogen at 1032.156 \AA blends with high-velocity absorption from O VI $\lambda 1031.926$, and absorption from the $J = 1$ level at 1038.156 \AA blends with high-velocity absorption from the O VI $\lambda 1037.617$, if the H_2 column densities are high enough. We employed a modeling process to decontaminate the data from blending by H_2 lines. We took all H_2 lines in the *FUSE* data with no major contamination or continuum placement uncertainties, and measured their equivalent widths. We then performed a curve-of-growth analysis for each rotational (J) level, and derived $\log N(\text{H}_2) = 13.72 \pm 0.15$, 13.99 ± 0.23 , < 13.89 , < 13.89 , and < 13.83 in levels $J = 0, 1, 2, 3$, and 4 respectively, corresponding to $\log N(\text{H}_2) \approx 14.34$ in total. This model is included in the continuum fits for contaminated *FUSE* absorption lines in Figure 2. Examination of the O VI $\lambda 1037.617$ panel shows significant contamination of the high-velocity absorption by H_2 $\lambda 1038.156$, and so we choose to base all measurements of high-velocity O VI on the strong O VI line.

Contamination from redshifted O VI $\lambda 1037.617$ absorption associated with the AGN itself ($z = 0.49246$) blends with low- and high-velocity C IV absorption in the 1548.195 \AA line. This associated absorber has a multiple-component structure and prevents a reliable measurement of high-velocity C IV $\lambda 1548.195$ absorption. We therefore concentrate on the weak line (1550.770 \AA) for measurements of high-velocity C IV absorption in this direction.

3.2. Blends toward PG 0953+414

Our measurement of the foreground H_2 absorption in the PG 0953+414 direction finds $\log N(\text{H}_2) = 13.90$, 14.40 , 14.00 , 14.12 , < 14.09 in levels $J = 0, 1, 2, 3$, and 4, giving a total $\log N(\text{H}_2) = 14.75$. As was the case for HE 0226–4110, H_2 $\lambda 1032.156$ at 125 km s^{-1} in the frame of O VI $\lambda 1031.926$ is predicted to be of negligible strength, but the $J = 1$ H_2 line at 1038.156 \AA (central line depth 0.27) blends with high-velocity absorption from the weak line of O VI at 1037.617 \AA (See Figure 5). We therefore adopt measurements of the strong line of O VI only.

There are few IGM systems near our lines of interest in the PG 0953+414 sight line. See Savage et al. (2002) for an investigation of the IGM absorption in this direction.

4. HIGH-VELOCITY ABSORPTION TOWARD HE 0226–4110

Our *FUSE* and *HST*/STIS observations of HE 0226–4110 reveal high-velocity absorption in lines of H I, C II, C III, C IV, O VI, Si II, Si III, and Si IV (Figure 2). Fe II is detected at low significance. No absorption is seen in N I, N II, O I, S II, S III, P II, Ar I, and Fe III. Multi-component structure is clearly seen in the HVCs in the Si II, Si III, C II, and C IV profiles observed at 7 km s^{-1} resolution. Based on component fits to these lines, we identify four positive-velocity components centered at 99, 148, 175, and 193 km s^{-1} , covering the ranges 80–125, 125–160, 160–185, and $185\text{--}230 \text{ km s}^{-1}$, and shown in Figure 4 with the colors purple, blue, green, and yellow respectively. Absorption in the 99 km s^{-1} component is distinct from the Galactic absorption centered at -10 km s^{-1} , so we treat this component as an HVC, even though the blueshifted parts of this component lie outside the formal definition of high-velocity ($|v_{LSR}| > 100 \text{ km s}^{-1}$).

Inspection of Figure 4 reveals the HVC component structure to be consistent among lines of different ionization states. We show the STIS data at full resolution here so that no kinematic information is lost. Tracers of neutral (C II, Si II), weakly ionized (Si III), and highly ionized gas (C IV, Si IV, O VI) show absorption over the same velocity range, and with a similar component structure. Among the high ions, the 99 (purple), 175 (green), and 193 km s^{-1} (yellow) components are clearest in O VI, C IV, and Si IV, respectively. This indicates that the high-ion/high-ion ratios differ between components. There are further differences between components in the low-ion/high-ion ratios; for example, $N(\text{Si II})/N(\text{Si IV})$ changes from > 2.0 at 145 km s^{-1} to 1.0 at 193 km s^{-1} .

The unblended O VI absorption in the 99 km s^{-1} component is broader than the corresponding lower ionization component; we measure $b(\text{O VI}) = 33 \pm 2 \text{ km s}^{-1}$ and $b(\text{C II}) = 16 \pm 3 \text{ km s}^{-1}$. The fact that high-velocity absorption is seen over a similar velocity extent in both neutral, weakly ionized, and highly ionized species indicates that common structures contain all these ions. However, the line widths imply that the neutral and highly ionized species are not co-spatial, and so *multiple phases* are required in each component.

The H I Lyman lines (Figure 3) show strong high-velocity absorption extending out to 230 km s^{-1} , the same extreme velocity as is seen in the O VI profile. We note that the H I column densities in the four HVCs toward HE 0226–4110 all lie between $10^{16.2}$ and $10^{16.7}$. Since H I clouds become optically thick to hydrogen ionizing radiation ($\lambda < 912 \text{ \AA}$) at $\log N(\text{H I}) \approx 17.2$, these HVCs are optically thin. Consequently, there should be little shielding of the HVC core, and we expect the ionizing radiation field to be relatively constant within the clouds.

5. HIGH-VELOCITY ABSORPTION TOWARD PG 0953+414

FUSE and STIS data of PG 0953+414 reveal high-velocity absorption in H I, C II, C III, C IV, Si III, Si IV, and O VI in the range $80\text{--}200 \text{ km s}^{-1}$, together with a narrow -146 km s^{-1} HVC seen in the lines of C II, Si II, and Si III (Figure 5, Table 4).

In the positive-velocity HVC, a single, narrow ($b = 10 \text{ km s}^{-1}$) neutral component at 124 km s^{-1} is clearly seen in the C II profile (Figure 7, blue shading), and at moderate significance (3.0σ) in the O I profile, though

no coincident Si II absorption is detected at significant levels. The C III and Si III profiles (green), tracing gas of intermediate ionization level, also show a component centered near 125 km s^{-1} , though the absorption in these species is much broader ($b = 40 \text{ km s}^{-1}$); the C III profile also contains a wing extending out to 200 km s^{-1} .

The highly ionized species C IV and Si IV (red) show weak absorption components centered near 150 km s^{-1} at detection significances of 2.7 and 2.3σ , respectively, displaced in velocity from the C III centroid by $\approx 25 \text{ km s}^{-1}$. The O VI profile in this direction shows a distinctive positive-velocity wing extending from 75 km s^{-1} out to 200 km s^{-1} . The wing is qualitatively different from the absorption profiles in neutral species, weakly ionized species, and the highly ionized species C IV and Si IV. Interestingly, there is more O VI absorption at velocities where H I is strongest ($80\text{--}125 \text{ km s}^{-1}$) than where C IV is strongest ($135\text{--}200 \text{ km s}^{-1}$); the $N(\text{C IV})/N(\text{O VI})$ ratio therefore changes with velocity over the range of the high-velocity absorption.

The negative-velocity HVC at -146 km s^{-1} is seen in lines of C II, Si II, Si III, and Si IV, all of which show b -values in the range $12\text{--}15 \text{ km s}^{-1}$. Although the H I absorption in this component appears to be blended with low-velocity absorption, we conclude high-velocity H I is present since our Voigt model without the -146 km s^{-1} component clearly does not fit the data (Figure 6). The -146 km s^{-1} HVC has the interesting property of no associated O VI or C IV absorption.

6. PHOTOIONIZATION MODELLING: THE CLOUD CORES

We used the 1-dimensional plane-parallel photoionization code CLOUDY (v94.00; Ferland et al. 1998) to model the HVCs as uniform density slabs exposed to an ionizing radiation field. The purpose of this exercise is to assess whether photoionization is a viable ionization mechanism, and if so, to provide information on the physical conditions and elemental abundances in the clouds. We consider two incident radiation fields: the extragalactic background (EGB) and the radiation field escaping from the Milky Way (MW).

6.1. Extragalactic Background Radiation

The extragalactic background (EGB) radiation contains enough ionizing photons to maintain the levels of ionization seen in many HVCs (Sembach et al. 2001a; Tripp et al. 2003; Collins et al. 2004, 2005; Ganguly et al. 2005). The EGB field we use is taken from Haardt & Madau (1996), who calculate the mean intensity J_ν as a function of wavelength at various redshifts by following the radiative transfer of a model QSO UV spectrum through the IGM (see their Figure 5). The EGB field at $z = 0$ has a mean intensity at the Lyman Limit (912 \AA) $J_\nu = 10^{-23} \text{ erg cm}^{-2} \text{ s}^{-1} \text{ Hz}^{-1} \text{ sr}^{-1}$, and is shown as the blue line on Figure 8.

A CLOUDY calculation requires a geometry in which the radiation field is plane-parallel and incident from one side of the cloud. For the EGB, the true field is isotropic, but since the HVCs under study are optically thin to Lyman continuum radiation, the *direction* of incident ionizing photons is unimportant. We therefore collapse the EGB field into a one-dimensional flux with the same energy density as the isotropic field ($F_\nu = 4\pi J_\nu$). When one divides F_ν by the photon energy $h\nu$ and integrates

from 0 to 912 Å, the EGB field at $z = 0$ is found to contain 10^4 hydrogen-ionizing (hard) photons $\text{cm}^{-2} \text{s}^{-1}$.

6.2. Escaping Milky Way Radiation

To determine the flux of escaping Galactic radiation, we first estimate the ionizing spectrum in the disk, and then consider what fraction of photons escape into the halo. The basic theory is outlined in Bland-Hawthorn & Maloney (1999) although we now present an extended model. First, the 90-912 Å region is dominated by O-B stars and these are confined to spiral arms (see Bland-Hawthorn & Maloney 2002). The unextinguished O-B star radiation field is normalized to the distribution of O stars near the solar circle compiled by Vacca, Garmany, & Shull (1996). The mean opacity in the 90-912 Å window is taken to be $\tau=2.8$, implying 6% of the hard O-B star photons escape into the halo normal to the disk. This escape fraction is established from the intensity of H α emission from HVCs with known distance bounds (Bland-Hawthorn & Maloney 1999, 2002; Putman et al. 2003b), assuming that the H α is photoionized.

Secondly, the disk spectrum in the range 912–2460 Å is derived from the observed spectrum in the solar neighbourhood (Mezger, Mathis, & Panagia 1982). Here we make a key assumption that the observed field at the Sun’s position has already been extinguished with a mean 912–2460 Å opacity of $\tau=1.5$. This takes account of the fact that some of the field will have originated close to the O-B stars, and some from stars which have moved away from the main star forming regions. We adopt the same opacity normal to the disk such that 22% of the soft UV photons escape into the halo.

The unextinguished 90-2460 Å ionizing spectrum in the disk is shown as the uppermost green line in Figure 8. The extinguished spectra at distances of 10, 50, and 100 kpc along the PG 0953+414 sight line are then shown with the lower curves. The geometry of both the hard and soft MW radiation fields is illustrated in Fig. 9, where the contours are lines of constant ionizing flux Φ , and the numbers given represent the logarithm of Φ in units of photons $\text{cm}^{-2} \text{s}^{-1}$. The Galactic hard radiation field dominates the EGB hard radiation inside the $\log \Phi = 4$ contour, which occurs at approximately 40 kpc for directions $|b| < 30^\circ$, 100 kpc for $30 < |b| < 60^\circ$, and 180 kpc for directions $|b| > 60^\circ$. We do not including ionizing photons from hot white dwarfs, planetary nebulae, and Galactic soft X-ray sources, which may affect the MW radiation field (Bregman & Harrington 1986), or ionizing photons from the Magellanic Clouds.

6.3. General Properties of Photoionization models: Galactic vs Extragalactic

In Figure 10 we plot $N(\text{C III})/N(\text{C II})$, $N(\text{C IV})/N(\text{C II})$, $N(\text{Si III})/N(\text{Si II})$, and $N(\text{Si IV})/N(\text{Si II})$ against U ($= n_\gamma/n_{\text{H}}$) for three photoionization cases: pure MW, pure EGB, and MW+EGB at 50 kpc toward HE 0226–4110. The differences between these curves are caused by the EGB being harder than the MW field. At $\log U \lesssim -2.0$, this leads to higher $N(\text{Si IV})/N(\text{Si II})$ and $N(\text{C IV})/N(\text{C II})$ ratios in the EGB. At $\log U \gtrsim -2$, the EGB begins to ionize silicon and carbon beyond Si IV and C IV,

resulting in the turnover in the EGB curves shown in Figure 10; the MW field produces Si IV and C IV as the dominant ionization stages at these ionization parameters. The results are robust to increasing the number of non-hydrogen-ionizing photons.

6.4. Modelling the HVCs toward HE 0226–4110 and PG 0953+414

We explicitly modeled each HVC absorption component toward HE 0226–4110 and PG 0953+414 by comparing the CLOUDY model predictions with the observed ionic column densities of carbon and silicon (summarized in Table 5), and determining the best-fit values of $\log U$ and metallicity $[Z/\text{H}]^6$. We assume all the H I exists in the same phase as the low ions. This is repeated for assumed HVC distances of 10, 50, and 100 kpc, with the Galactic radiation field scaled appropriately using Figure 9. At each distance we add the uniform EGB contribution and enter the combined field into CLOUDY (we do not account for the attenuation of EGB photons passing through the H I disk of the Milky Way). Table 6 shows the flux of the radiation field with distance along the sight lines to HE 0226–4110 and PG 0953+414.

6.4.1. Low versus High Ions

For all HVCs toward both HE 0226–4110 and PG 0953+414, and for both EGB and MW radiation fields, we found we could reproduce the column densities of the singly- and doubly-ionized species (i.e., C II, C III, Si II, Si III), but not the triply-ionized species (C IV and Si IV) or the O VI. In Figure 11 we show the results from an example run, (HVC2 toward PG 0953+414), for two different radiation field cases (EGB and MW at 10 kpc). The observations are shown as the larger data points, with 1σ error bars. For either MW or EGB fields, the observed levels of Si IV, C IV, and O VI are significantly (at least 1 dex) higher than the photoionization model predicts at the value of U which explains the singly and doubly ionized species. The underproduction of the high ions is worse for the MW case. We attempted separate high-ion only models, but found that we could not simultaneously reproduce the observed $N(\text{Si IV})$, $N(\text{C IV})$, and $N(\text{O VI})$ with one value of U . *These results strongly suggest that Si IV, C IV, and certainly O VI are not photoionized in these HVCs.* The difficulty in photoionizing O VI has been reported elsewhere, both in the modelling of observed HVC ionization patterns (S03, Collins et al. 2004, 2005; Ganguly et al. 2005) and in theoretical work on the structure of photoionized clouds (Kepner et al. 1999; Gnat & Sternberg 2004).

Given that the species which appear most consistent with photoionization are C II, C III, Si II, and Si III, we derive our best-fit values of $\log U$ and metallicity $[Z/\text{H}]$ (assuming a solar Si/C ratio) for each component by minimizing the χ^2 statistic using data from these four ions only. By investigating the depth of the χ^2 minima, we find typical errors on $\log U$ and $[Z/\text{H}]$ of ± 0.2 dex (95%

⁶ $[Z/\text{H}] = \log(N_Z/N_{\text{H}}) - \log(N_Z/N_{\text{H}})_\odot$. The relevant solar abundances we adopt throughout this section, using the definition $A_X = n(X)/n(\text{H})$, are: $\log A_{\text{C}} = -3.61$ (Allende Prieto, Lambert, & Asplund 2002); $\log A_{\text{N}} = -4.07$ (Holweger 2001); $\log A_{\text{O}} = -3.34$ (Asplund et al. 2004); $\log A_{\text{Si}} = -4.46$ (Holweger 2001); $\log A_{\text{Fe}} = -4.55$ (Holweger 2001).

c.l.). By combining $[Z/H]$ and $\log U$ with the temperature and ionization breakdown for each ion returned by the CLOUDY model, we derive the following quantities for the HVCs (see Table 7): gas density, physical size, thermal pressure, hydrogen ionization fraction, and predicted intensity $H\alpha$ emission.

For a given component, the closer the clouds are assumed to be to the Milky Way, the higher their density, pressure, and predicted $H\alpha$ intensity, and the smaller their physical depth. The temperature of the photoionized clouds remains confined to a range between $1.0\text{--}2.2 \times 10^4$ K.

6.4.2. HVCs toward HE 0226–4110

For the four HVC components toward HE 0226–4110, we find overall metallicities of -0.6 ± 0.2 , -0.4 ± 0.2 , -0.9 ± 0.3 , and -0.6 ± 0.2 ; these derived abundances are essentially independent of the assumed distance to the clouds. Elemental abundance studies of the Magellanic Stream, lying eleven degrees away from the HE 0226–4110 sight line, have found $[\text{Si}/\text{H}] = -0.8 \pm 0.2$ in the Leading Arm (Sembach et al. 2001b), and $[\text{Si II}/\text{H}] \gtrsim -1.5$ in the main body of the stream (Gibson et al. 2000). Magellanic Stream abundances are similar to those in the Small Magellanic Cloud⁷, characterized by $[\text{Si}/\text{H}]_{\text{SMC}} = -0.51$, $[\text{C}/\text{H}]_{\text{SMC}} = -0.66$; (Russell & Dopita 1992, corrected to our updated solar abundance scheme). Since our derived values for the silicon abundances in the HVCs toward HE 0226–4110 are suggestive of a Magellanic Stream origin, we are able to place the HVCs at ≈ 50 kpc. Looking at the inferred densities, pressures, and cloud sizes of the MW+EGB 50 kpc models of the HE 0226–4110 clouds in Table 7, we find that the four HVCs have derived densities in the range $\log n_{\text{H}} = -2.3$ to -2.1 , physical sizes of 39 to 120 pc, thermal pressures of $95\text{--}190 \text{ cm}^{-3} \text{ K}^8$, and hydrogen ionization fractions of 98%. If we assume spherical symmetry for the clouds, they have masses in the range $10\text{--}250 M_{\odot}$ and angular sizes on the sky of several arcminutes. Other geometries could result in substantially larger values for both the mass and angular size. One explanation is that the clouds trace material tidally stripped from the main (21-cm) body of the Magellanic Stream, which are then ionized by the pervading MW radiation field.

If we treat the detection of Fe II in HVC2 at 2.4σ significance as real, then the CLOUDY model returns $[\text{Fe}/\text{H}] \approx +0.6$ in this component, whereas carbon and silicon give $[Z/H] = -0.4$. We note that Lu et al. (1998) concluded that dust was present in the Magellanic Stream, since the measured S/Fe ratio of eight times the solar value in HVC 287.5+22.5+240 requires much of the iron to be depleted out of the gas phase. Unless the elemental abundances are markedly different in the core toward HVC 287.5+22.5+240 than in the HVCs under study here, we conclude that the iron feature in HVC2 is likely not real; it could be due to fixed pattern noise.

Collins et al. (2005) report a size of 5.9 kpc for the same HVC system toward HE 0226–4110 that we model

⁷ In the Gardiner & Noguchi (1996) tidal model, all the gas in the Magellanic Stream comes out of the SMC.

⁸ The main body of the Stream contains clumps with higher thermal pressure: Sembach et al. (2001b) measure $P/k \sim 360 \text{ cm}^{-3} \text{ K}$ in the leading-arm.

here, based on different photoionization models. The difference between their result and ours (HVC sizes of 39–120 pc if the clouds are at 50 kpc) is partly due to their modeling the system as a single component, whereas we use four components, with smaller individual column densities. A second reason is metallicity: we derive values higher than the 0.1 solar assumed by Collins et al. (2005), resulting in our finding lower ionization parameters, higher densities, and smaller cloud sizes.

6.4.3. HVCs toward PG 0953+414

The metallicity of the 125 km s^{-1} HVC toward PG 0953+414 is $[Z/H] = -0.8 \pm 0.2$ independent of distance, suggesting it is not a fountain cloud, which would be expected to have solar metallicity or above, but rather a cloud of non-Galactic origin that happens to be moving away from the LSR. Our modeling finds the cloud to be 99–100% ionized. The detection of O I at apparent 3.0σ significance in HVC2 implies $[\text{O I}/\text{H I}] \approx [\text{O}/\text{H}] = +0.6 \pm 0.2$ if the feature is real. Since the carbon and silicon lines suggest metallicities lower by ≈ 1.6 dex, this O I detection is likely spurious. We have no information on the distance to this absorber.

The -146 km s^{-1} HVC has a metallicity of -0.6 ± 0.2 . The Si II/Si III and Si II/C II column density ratios (and overall line strengths) in the -150 km s^{-1} HVC toward PG 0953+414 are similar to those of the $+100 \text{ km s}^{-1}$ HVC in the spectrum of PG 1116+215 recently presented by Ganguly et al. (2005). The properties of both of these HVCs, including these low-ion ratios, the absence of C IV and O VI, and the approximate H I columns, are highly reminiscent of the Virgo Cluster Ly α cloud in the spectrum of 3C 273.0 at $z_{\text{abs}} = 0.00530$ (Sembach et al. 2001a; Tripp et al. 2002). Tripp et al. find that the 3C 273.0 Ly α cloud is quite small, ~ 70 pc, of the same order as the sizes we derive for the -146 km s^{-1} HVC (80 pc if at 100 kpc). Tumlinson et al. (2005) report two Ly α absorbers toward QSO PG 1211+143, each lying within 150 kpc of a potential host galaxy, which also have ionization properties similar to those of Galactic highly ionized HVCs.

6.5. HVC Thermal Pressure

We compare our derived HVC pressures with the estimated pressure of an isothermal Galactic corona, as a function of distance. The coronal pressure has been calculated by Sternberg, McKee, & Wolfire (2002) for a 2×10^6 K hydrostatic halo using a two-component (disk and dark-matter) Galactic potential. Sternberg et al. find $P_{\text{HIM}}/k \approx [1000, 250, 100] \text{ cm}^{-3} \text{ K}$ at $r = [10, 50, 100]$ kpc. By averaging the results of the six HVCs we model, we find a typical P/k of $[530, 140, 50] \text{ cm}^{-3} \text{ K}$ if the clouds are at these same distances. Ignoring the difference between the Sun-HVC and Galactic Center-HVC distances, our clouds would therefore be slightly underpressurized in a 2×10^6 K corona, but would be close to thermal pressure equilibrium in a 1×10^6 K corona. Such a medium is suspected from UV (S03, Fox et al. 2004; Collins et al. 2004, 2005; Ganguly et al. 2005) and X-ray high-ion absorption (Fang et al. 2003; McKernan, Yaqoob, & Reynolds 2004) studies, and from pulsar dispersion measures, X-ray emission, and properties of the Magellanic Stream (see Quilis & Moore 2001, and references therein). At 50 kpc, the density of a fully

ionized 10^6 K corona would be $n_{\text{H}} = 4 - 9 \times 10^{-5} \text{ cm}^{-3}$ if thermal pressure equilibrium holds in the HVCs toward HE 0226–4110, assumed to be part of the Magellanic Stream. Magnetic fields and cosmic rays may also provide pressure confinement, but the similarity of thermal pressures between a hot corona and these HVCs is striking nonetheless.

7. COLLISIONAL IONIZATION: THE CLOUD BOUNDARIES

Since photoionization cannot explain the high ions, we now investigate collisional ionization models, specifically: collisional ionization equilibrium (CIE; Sutherland & Dopita 1993), magnetized conductive interfaces (CIs; Borkowski et al. 1990), turbulent mixing layers (TMLs; Slavin et al. 1993), radiatively cooling hot gas (RC; Edgar & Chevalier 1986), and shock ionization (SI; Dopita & Sutherland 1996). A brief description of each of these models, and the appropriate range of their parameter space, is given in Fox et al. (2004).

To increase the sample of observations over the high-ion detections in HVCs toward HE 0226–4110 and PG 0953+414, we produce a compilation of all measurements of highly ionized HVCs where Si IV, C IV, and N V data exist (Fox et al. 2004; Collins et al. 2004; Ganguly et al. 2005). This compilation is presented in Table 8. In cases where only a limit could be measured for $N(\text{Si IV})$, $N(\text{C IV})$ or $N(\text{N V})$, we present a corresponding 3σ upper limit to the ratio of that ion to O VI. We calculate the mean and standard deviation of the high ion ratios in these fourteen HVCs, and compare these to the integrated averages measured in the Galactic halo (Zsargó et al. 2003).

There is an enormous range in $N(\text{H I})/N(\text{O VI})$ observed in HVCs, from $\sim 10^6$ in Complex C to $\sim 10^2$ in components toward PG 0953+414 and PKS 2155–304. The variation in the ratio is primarily due to variations in $N(\text{H I})$, whereas $N(\text{O VI})$ is always found to be within 1 dex of 13.0. This represents a crucial piece of evidence in understanding the structure of HVCs: no matter how much neutral gas there is, some process regulates the production of highly ionized gas and always produces a similar amount of O VI. A corresponding dispersion in the $N(\text{H I})/N(\text{O VI})$ ratio in low redshift intergalactic O VI absorbers has been noted (Tripp, Savage, & Jenkins 2000; Danforth & Shull 2005).

Our observations are compared with the model predictions in Figure 12, which contains plots of $N(\text{C IV})/N(\text{O VI})$ vs $N(\text{N V})/N(\text{O VI})$ (left panel), and $N(\text{Si IV})/N(\text{O VI})$ vs $N(\text{N V})/N(\text{O VI})$ (right panel). All measurements of high-ion column density ratios in HVC components (given in Table 8) are shown in red, upper limits are shown in purple, and the Galactic halo average is shown in green (Zsargó et al. 2003). The shaded regions represent the range of parameter space allowed by the various models. The blue arrows show the effect of correcting the model predictions to a scheme of SMC abundances (Russell & Dopita 1992), assuming that oxygen is the dominant coolant (see Fox et al. 2004, for a description of the correction process). A summary of the ability of each model to reproduce the observations is summarized in Table 9.

The shock ionization model, when calculated using a shock speed of 200 km s^{-1} (closest to the LSR velocities of

the HVCs toward HE 0226–4110 and PG 0953+414) systematically underestimates $N(\text{C IV})/N(\text{O VI})$. A much higher velocity shock ($\sim 500 \text{ km s}^{-1}$) is needed to explain the $N(\text{C IV})/N(\text{O VI})$ ratio by shock ionization, which makes this scenario unlikely, though we cannot rule it out, since a HVC falling in at 200 km s^{-1} against a 300 km s^{-1} Galactic outflow would produce a relative velocity of $\sim 500 \text{ km s}^{-1}$, and hence a higher Mach number. The region of ratio-ratio space in Figure 12 covered by the shock model prediction allows for the possibility of shock velocities of up to 500 km s^{-1} .

Conductive interfaces can explain the $N(\text{C IV})/N(\text{O VI})$ and $N(\text{N V})/N(\text{O VI})$ ratios in almost all cases, but cannot explain the $N(\text{Si IV})/N(\text{O VI})$ observations. However, less weight should be given to the ratios involving $N(\text{Si IV})$. Ionizing photons produced in the interface itself (Sembach & Savage 1992; Slavin 2004) might inflate $N(\text{Si IV})$, rendering the purely collisional ionization model predictions invalid. In particular, the interface should be a strong emitter of He II $\lambda 304$ radiation, capable of ionizing Si IV but not C IV (Sembach & Savage 1992; Savage, Sembach, & Cardelli 1994). Such ionizing photons are *not* accounted for in our CLOUDY photoionization models of §6. In the case where all ratios involving $N(\text{Si IV})$ are ignored, the conductive interface model is the most successful at explaining the remaining ratios (C IV/O VI and N V/O VI) in HVCs (and the average Galactic halo value). The interface model is also consistent with the observed HVC absorption kinematics, since the observed high ion-low ion offsets are of the same order ($0\text{--}25 \text{ km s}^{-1}$) as would be expected in an evaporative flow off a conductive interface (Böhringer & Hartquist 1987).

To further our understanding of conductive interfaces, the effects of HVC motion on the conduction across the interface need to be explored theoretically. Numerical simulations of the interaction between infalling HVCs and surrounding media (Quilis & Moore 2001; Murray & Lin 2004) indicate that cometary features, turbulence, and bow shocks are all expected to occur around HVCs. More advanced models of conductive interfaces would also allow for a full treatment of the ionizing radiation produced within the interface itself (the diffuse field; Ferrara & Field 1994; Slavin 2004). Such a treatment would be able to make predictions on the relationship between HVC O VI absorption and HVC H α emission (Weiner & Williams 1996; Tufté, Reynolds, & Haffner 1998; Tufté et al. 2002; Putman et al. 2003b). If a significant fraction of the H α emission from HVCs arises from conductive interfaces, rather than by photoionization from escaping Galactic radiation, then the true escape fraction of Galactic ionizing photons may be less than the 6% (normal to disk) discussed in §6. Further H α studies of HVCs will help elucidate this issue.

8. POSITIVE-VELOCITY WINGS

The O VI profile toward PG 0953+414, with its smooth positive-velocity wing rather than discrete component, is qualitatively different from the C II, C III, C IV, Si III, and Si IV absorption line profiles in this direction. The C IV and Si IV HVCs, although observed at low significance, each appear to show a broad component cen-

tered near 150 km s^{-1} . One interpretation of the data is that the 125 km s^{-1} HVC (seen in C II) is surrounded by highly ionized interface layers, which contain the ions C IV and Si IV. This explanation is consistent with the C IV/Si IV ratio, the C IV–C II offset, and our explanation for the high ions in the HE 0226–4110 clouds and other HVCs, but poses the question: where is the O VI in this interface? We show using the blue line in the upper-right panel of Figure 7 that the interface O VI could well be hiding underneath the wing. This line shows the contribution to the O VI profile of an interface component having the same width as the C IV HVC and a typical $N(\text{C IV})/N(\text{O VI})$ interface ratio (of 1). As can be seen, such a component can explain all the O VI absorption between 140 and 200 km s^{-1} , but *not the remaining high-velocity O VI between 75 and 140 km s^{-1} .*

The O VI seen at 75 – 140 km s^{-1} toward PG 0953+414 has no accompanying absorption seen in C IV or Si IV: we find $\log N(\text{O VI}) = 13.67 \pm 0.08$, $\log N(\text{C IV}) < 13.22$, and $\log N(\text{Si IV}) < 12.49$ over the same velocity range. Assuming solar C/O and Si/O ratios and CIE conditions apply, the C IV/O VI and Si IV/O VI ratios imply $\log T > 5.31$ and > 5.26 , respectively. This hot gas may be tracing a hot Galactic Fountain (Shapiro & Field 1976; Bregman 1980; Norman & Ikeuchi 1989; Houck & Bregman 1990): a circulation of interstellar material in which supernovae-heated gas rises buoyantly into the halo, cools, and then rains back toward the disk. In a hot fountain, little O VI is expected in the initial 10^6 K flow, but as the gas cools, higher stages of ionization will recombine into O^{+5} as the flow drives outward, even though gas at $3 \times 10^5 \text{ K}$ (where O VI is formed by collisions) is not hot enough to drive the flow. The model is attractive for explaining positive-velocity wings since it naturally explains why the wings are always seen to be redshifted; no negative-velocity (in-falling) wings are seen in O VI profiles.

The Galactic Fountain model has had some success explaining the kinematics and metallicities of the intermediate velocity clouds (IVCs), defined to be at $|v_{LSR}| = 30$ – 90 km s^{-1} (Richter et al. 2001). One could speculate that hot outflowing fountain gas is detected as positive-velocity wings, and cooler inflowing gas is detected in the form of neutral IVCs. In this case, the outflowing gas must be dense enough to cool in the time it takes to rise out into the halo, otherwise the H I IVCs will never condense. Since the instantaneous radiative cooling time is $t_{cool} = 2.4 \times 10^8 n_{-3}^{-1} T_6 \Lambda_{-21.9}^{-1} \text{ yr}$ (Houck & Bregman 1990), where $\Lambda_{-21.9}$ is the cooling function in units of its value at 10^6 K ($1.26 \times 10^{-22} \text{ erg cm}^3 \text{ s}^{-1}$), $T_6 \equiv T/10^6 \text{ K}$, and $n_{-3} \equiv n/10^{-3} \text{ cm}^{-3}$, we find that a 10^6 K fountain flow moving at 100 km s^{-1} must have a density $n_{-3} \approx 9$ to radiate half its internal energy in a sound crossing time (28 Myr for a scale height of 2.5 kpc, appropriate for an isothermal 10^6 K halo), which approximates the time taken for the gas to fill the halo.

A related possibility is that the wings trace an escaping Galactic wind, energetic enough to escape the Galactic potential well. Cosmic rays could play a role in driving such a Galactic wind and supporting high- z gas (Breitschwerdt, McKenzie, & Völk 1991). O VI-containing outflows are predicted by hydrodynamical simulations of galaxy winds (Mac Low & Ferrara 1999; Strickland & Stevens 2000), and have been detected in

starburst galaxies NGC 1705 (Heckman et al. 2001) and NGC 625 (Cannon et al. 2005). Mid-infrared images of the Galactic center show a large-scale bipolar outflow in our own galaxy (Bland-Hawthorn & Cohen 2003). Analysis of a larger sample of positive-velocity wings will be necessary to fully explore the properties of an O VI outflow.

9. SUMMARY

We have studied *FUSE* and *HST/STIS* spectra to investigate the ionization, kinematics, elemental abundances, and physical conditions in the HVCs toward HE 0226–4110 and PG 0953+414. We summarize our study in the following key points.

- HVCs toward HE 0226–4110.** HVC absorption in the range 80 – 230 km s^{-1} is detected in the HE 0226–4110 direction in lines of H I, C II, C III, C IV, O VI, Si II, Si III, and Si IV. Four components are clearly seen in this velocity range in the high-resolution STIS observations of C II, Si II, and Si III, at 99 , 148 , 175 , and 193 km s^{-1} . Each of these components is accompanied by a broader, highly ionized (C IV or O VI) component, indicating that warm and hot phases exist in each component. The warm high-velocity clouds are all found to have similar densities, pressures, physical sizes, and ionization levels; their metallicities ($[Z/H]$ between -0.9 and -0.4) indicate the clouds may be outlying fragments of the Magellanic Stream, whose main body lies 11° away on the sky at similar velocities to the HE 0226–4110 absorbers.
- HVCs toward PG 0953+414.** HVCs exist at both negative and positive velocities toward PG 0953+414. The negative-velocity HVC at -146 km s^{-1} is seen in C II, Si II, Si III, and Si IV, has $[Z/H] = -0.6 \pm 0.2$, and contains no detectable C IV or O VI. At positive velocities, a narrow discrete HVC component with $[Z/H] = -0.8 \pm 0.2$ is seen in C II at 124 km s^{-1} . C III and Si III show much broader absorption components centered at the same velocity. The highly ionized species Si IV and C IV show a weak component near to 150 km s^{-1} , offset from the lower ionization species by $\sim 25 \text{ km s}^{-1}$. The O VI profile contains a smooth positive-velocity wing extending from 75 – 200 km s^{-1} . We show that part of this O VI absorption could be produced in the same absorber that contains C IV and Si IV, but the gas in the range 75 – 140 km s^{-1} requires an alternative explanation.
- CLOUDY Photoionization Modeling.** The Galactic ionizing radiation field from hot stars dominates the EGB ionizing radiation inside the $\log \Phi_{<912} = 4$ contour, which occurs at approximately 40 kpc for directions $|b| < 30^\circ$, 100 kpc for $30 < |b| < 60^\circ$, and 180 kpc for directions $|b| > 60^\circ$. Photoionization is a good explanation for the C II, C III, Si II, and Si III in the HVCs. Neither the EGB or the MW field can account for C IV and O VI in the HVCs, confirming that they exist in a separate, hotter gas phase.

4. Highly Ionized HVC Components. After studying the ionic column density ratio and kinematic information of thirteen highly ionized HVC components reported here and in the literature, we believe the highly ionized HVC components arise at the interfaces between the cool/warm HVCs and a surrounding medium. Conductive interfaces can reproduce $N(\text{C IV})/N(\text{O VI})$ and $N(\text{N V})/N(\text{O VI})$ in 11/12 highly ionized HVCs, though there are discrepancies remaining to be resolved with the $N(\text{Si IV})$ prediction. HVC high-ion column density ratios are not significantly different from the Galactic Halo averages of Zsargó et al. (2003), suggesting that similar ionization processes are at work in both environments. The interface scenario implies the existence of a hot, extended corona to the Milky Way extending out 50 kpc to the Magellanic Clouds. Such a corona can also provide confinement to the warm HVCs; our modelling shows the HE 0226–4110 HVCs would be close to pressure equilibrium in a fully ionized 10^6 K corona with $n_{\text{H}} = 4 - 9 \times 10^{-5} \text{ cm}^{-3}$ at 50 kpc.

5. Positive-Velocity Wings. The extended O VI absorption wing seen between 75 and 140 km s^{-1} toward PG 0953+414 may trace a hot Galactic outflow, because of the asymmetric profile and the lack of accompanying wing absorption in less-ionized species. The lack of C IV and Si IV in this velocity range can be used to constrain the temperature in the wing gas to be $\log T > 5.31$, assuming CIE and solar elemental abundance ratios.

The authors acknowledge an anonymous referee for a perceptive report. We thank Marilyn Meade for running the CALFUSE pipeline. The STIS observations of HE 0226–4110 were obtained for HST program 9148, with financial support through NASA grant HST-GO-9184.08-A from the Space Telescope Science Institute. BPW was supported by NASA grants NNG04GD85G and NAG5-7444. BDS acknowledges support from NASA grant NNG04GC70G. TMT appreciates additional support from NASA LTSA grant NNG04GG73G.

REFERENCES

- Allende Prieto, C., Lambert, D. L., & Asplund, A. 2002, *ApJ*, 573, L137
- Asplund, M., Grevesse, N., Sauval, A. J., Allende Prieto, C., Kiselevich, D. 2004, *A&A*, 417, 751
- Bland-Hawthorn, J., Veilleux, S., Cecil, G. N., Putman, M. E., Gibson, B. K., & Maloney, P. R. 1998, *MNRAS*, 299, 611
- Bland-Hawthorn, J., & Maloney, P. R. 1999, *ApJ*, 510, L33
- Bland-Hawthorn, J., & Maloney, P. R. 2002, in *Extragalactic Gas at Low Redshift*, ASP Conf. Ser. Vol. 254, eds. J. S. Mulchaey & J. T. Stocke, 267
- Bland-Hawthorn, J., & Cohen, M. 2003, *ApJ*, 582, 246
- Böhringer, H., & Hartquist, T. W. 1987, *MNRAS*, 228, 915
- Borkowski, K. J., Balbus, S. A., & Fristrom, C. C. 1990, *ApJ*, 355, 501
- Bowers, C. W., et al. 1998, *Proc. SPIE*, 3356, 401
- Braun, R., & Thilker, D. 2004, *A&A*, 417, 421
- Bregman, J. N. 1980, *ApJ*, 236, 577
- Bregman, J. N. 1980, & Harrington, J. P. 1986, *ApJ*, 309, 833
- Breitschwerdt, D., McKenzie, J. F., & Völk, H. J. 1991, *A&A*, 245, 79
- Brüns, C., Kerp, J., Staveley-Smith, L., Mebold, U., Putman, M. E., Haynes, R. F., Kalberla, P. M. W., Müller, E., & Filipovic, M. D. 2005, *A&A*, 432, 45
- Cannon, J. M., Skillman, E. D., Sembach, K. R., & Bomans, D. J. 2005, *ApJ*, 618, 247
- Collins, J. A., Shull, J. M., & Giroux, M. L. 2004, *ApJ*, 605, 216
- Collins, J. A., Shull, J. M., & Giroux, M. L. 2005, *ApJ*, in press (astro-ph/0501061)
- Danforth, C. W., & Shull, J. M. 2005, in *Astrophysics in the Far Ultraviolet*, ASP Conf. Ser., eds. H. W. Moos & G. Andersson, in press (astro-ph/0408262)
- Dopita, M. A., & Sutherland, R. S. 1996, *ApJS*, 102, 161
- Edgar, R. J., & Chevalier, R. A. 1986, *ApJ*, 310, L27
- Fang, T. T., Sembach, K. R., & Canizares, C. R. 2003, *ApJ*, 586, L49
- Ferland, G. J., Korista, K. T., Verner, D. A., Ferguson, J. W., Kingdon, J. B., & Verner, E. M. 1998, *PASP*, 110, 761
- Ferrara, A., & Field, G. B. 1994, *ApJ*, 423, 665
- Fox, A. J., Savage, B. D., Wakker, B. P., Sembach, K. R., Richter, P., & Tripp, T. M. 2004, *ApJ*, 602, 738
- Ganguly, R., Sembach, K. R., Tripp, T. M., & Savage, B. D. 2005, *ApJS*, 157, 251
- Gardiner, L. T., & Noguchi, M. 1996, *MNRAS*, 278, 191
- Gibson, B. K., Giroux, M. L., Penton, S. V., Putman, M. E., Stocke, J. T., & Shull, J. M. 2000, *AJ*, 120, 1830
- Gnat, O., & Sternberg, A. 2004, *ApJ*, 608, 229
- Haardt, F. & Madau, P. 1996, *ApJ*, 461, 20
- Heckman, T. M., Sembach, K. R., Meurer, G. R., Strickland, D. K., Martin, C. L., Calzetti, D., & Leitherer, C. 2001, *ApJ*, 554, 1021
- Heckman, T. M., Norman, C. A., Strickland, D. K., & Sembach, K. R. 2002, *ApJ*, 577, 691
- Holweger, H. 2001, in *AIP Conference Proceeding 598*, Solar and Galactic Composition, ed. R. F. Wimmer-Schweingruber (New York: AIP), 23
- Houck, J. C., & Bregman, J. N. 1990, *ApJ*, 352, 506
- Hulsbosch, A. N. M., & Wakker, B. P. 1988, *A&AS*, 75, 191
- Jenkins, E. B., & Tripp, T. M. 2001, *ApJS*, 137, 297
- Kepner, J., Tripp, T. M., Abel, T., & Spergel, D. 1999, *AJ*, 117, 2063
- Kim Quijano, J. et al. 2003, *STIS Instrument Handbook*, (Baltimore: STScI)
- Kimble, R. A., et al. 1998, *ApJ*, 492, L83
- Landsman, W., & Bowers, C. W. 1997, in *HST Calibration Workshop with a New Generation of Instruments*, eds. S. Casertano, R. Jedrzejewski, C. D. Keyes, & M. Stevens (Baltimore: STScI), 132
- Lehner, N., Savage, B. D., Wakker, B. P., Sembach, K. R., & Tripp, T. M. 2005, *ApJ*, in prep.
- Lu, L., Savage, B. D., Sembach, K. R., Wakker, B. P., Sargent, W. L. W., & Oosterloo, T. A. 1998, *AJ*, 115, 162
- Mac Low, M.-M., & Ferrara, A. 1999, *ApJ*, 513, 142
- McKernan, B., Yaqoob, T., & Reynolds, C. S. 2004, *ApJ*, 617, 232
- Mezger, P. G., Mathis, J. S., & Panagia, N. 1982, *A&A*, 105, 372
- Moos, H. W., et al. 2000, *ApJ*, 538, L1
- Morras, R., Bajaja, E., Arnal, E. M., & Pöppel, W. G. L. 2000, *A&AS*, 142, 25
- Morton, D. C. 2003, *ApJS*, 149, 205
- Muller, C. A., Oort, J. H., & Raimond, E. 1963, *C. R. Acad. Sci. Paris*, 257, 1661
- Murphy, E. M., et al. 2000, *ApJ*, 538, L35
- Maller, A. H., & Bullock, J. S. 2004, *MNRAS*, 355, 694
- Murray, S. D., & Lin, D. N. C. 2004, *ApJ*, 615, 586
- Norman, C., & Ikeuchi, S. 1989, *ApJ*, 345, 372
- Oort, J. H. 1970, *A&A*, 7, 381
- Pisano, D. J., Barnes, D. G., Gibson, B. K., Staveley-Smith, L., Freeman, K. C., & Kilborn, V. A. 2004, *ApJ*, 610, L17
- Putman, M. E., Staveley-Smith, L., Freeman, K. C., Gibson, B. K., & Barnes, D. G. 2003a, *ApJ*, 586, 170
- Putman, M. E., Bland-Hawthorn, J., Veilleux, S., Gibson, B. K., Freeman, K. C., & Maloney, P. R. 2003b, *ApJ*, 597, 948
- Quilis, V., & Moore, B. 2001, *ApJ*, 555, L95
- Richter, P., Sembach, K. R., Wakker, B. P., Savage, B. D., Tripp, T. M., Murphy, E. M., Kalberla, P. M. W., & Jenkins, E. B. 2001, *ApJ*, 559, 318
- Russell, S. C., & Dopita, M. A. 1992, *ApJ*, 384, 508

TABLE 1
SIGHT LINE PROPERTIES

Target	Type	z	l ($^{\circ}$)	b ($^{\circ}$)	V (mag.)	F_{1030}^a (flux units)	Δv_{LSR}^b (km s^{-1})
HE 0226-4110	Sey1	0.495	253.94	-65.78	15.2	2.7	-14.3
PG 0953+414	Sey1	0.234	179.79	+51.71	14.5	5.1	-0.3

NOTE. — Information retrieved from the NED database (<http://nedwww.ipac.caltech.edu>), unless noted below.

^aMeasured flux at 1030 Å; 1 flux unit = $10^{-14} \text{ erg cm}^{-2} \text{ s}^{-1} \text{ Å}^{-1}$.

^bCorrection from heliocentric to LSR velocity frame. $\Delta v_{LSR} = v_{LSR} - v_{Helio}$.

- Sahnou, D., et al. 2000, ApJ, 538, L7
Savage, B. D., & Sembach, K. R. 1991, ApJ, 379, 245
Savage, B. D., Sembach, K. R., & Cardelli, J. A. 1994, ApJ, 420, 183
Savage, B. D., Sembach, K. R., Tripp, T. M., & Richter, P. 2002, ApJ, 564, 631
Savage, B. D., et al. 2003, ApJS, 146, 125
Savage, B. D., Wakker, B. W., Fox, A. J., & Sembach, K. R. 2005a, ApJ, 619, 863
Savage, B. D., Lehner, N., Wakker, B. W., Sembach, K. R., & Tripp, T. M. 2005b, ApJ, in press (astro-ph/0503051)
Sembach, K. R., & Savage, B. D. 1992, ApJS, 83, 147
Sembach, K. R., Savage, B. D., Lu, L., & Murphy, E. M. 1995, ApJ, 451, 616
Sembach, K. R., Savage, B. D., Lu, L., & Murphy, E. M. 1999, ApJ, 515, 108
Sembach, K. R., et al. 2000, ApJ, 538, L31
Sembach, K. R., Howk, J. C., Savage, B. D., Shull, J. M., & Oegerle, W. R. 2001a, ApJ, 561, 573
Sembach, K. R., Howk, J. C., Savage, B. D., & Shull, J. M., 2001b, AJ, 121, 992
Sembach, K. R., et al. 2003, ApJS, 146, 165 (S03)
Shapiro, P. R., & Field, G. B. 1976, ApJ, 205, 762
Slavin, J. D., Shull, J. M., & Begelman, M. C. 1993, ApJ, 407, 83
Slavin, J. D. 2004, in ASSL Conference Proceedings Vol. 309: Soft X-Ray Emission from Clusters of Galaxies and Related Phenomena, eds R. Lieu & J. Mittaz (Dordrecht: Kluwer), 93
Sternberg, A., McKee, C. F., & Wolfire, M. G. 2002, ApJS, 143, 419
Strickland, D. K., & Stevens, I. R. 2000, MNRAS, 314, 511
Sutherland, R. S., & Dopita, M. A. 1993, ApJS, 88, 253
Tripp, T. M., Savage, B. D., & Jenkins, E. B. 2000, ApJ, 534, L1
Tripp, T. M., Giroux, M. L., Stocke, J. T., Tumlinson, J., & Oegerle, W. R. 2001, ApJ, 563, 724
Tripp T. M., et al. 2002, ApJ, 575, 697
Tripp T. M., et al. 2003, AJ, 125, 3122
Tuftte, S. L., Reynolds, R. J., & Haffner, L. M. 1998, ApJ, 504, 773
Tuftte, S. L., Wilson, J. D., Madsen, G. J., Haffner, L. M., & Reynolds, R. J. 2002, ApJ, 572, L153
Tumlinson, J., Shull, J. M., Giroux, M. L., & Stocke, J. T. 2005, ApJ, 620, 95
Vacca, W. D., Garmany, C. D., & Shull, J. M. 1996, ApJ, 460, 914
Wakker, B. P. & van Woerden, H. 1997, ARA&A, 35, 217
Wakker, B. P., et al. 1999, Nature, 402, 388
Wakker, B. P., Kalberla, P. M. W., van Woerden, H., de Boer, K. S., & Putman, M. E. 2001, ApJS, 136, 537
Wakker, B. P., et al. 2003, ApJS, 146, 1
Weiner, B. J., & Williams, T. B. 1996, AJ, 111, 1156
Welsh, B. Y., Sfeir, D. M., Sirk, M. M., & Lallement, R. 1999, A&A, 352, 308
Woodgate, B. E., et al. 1998, PASP, 110, 1183
Zsargó, J., Sembach, K. R., Howk, J. C., & Savage, B. D. 2003, ApJ, 586, 1019

TABLE 2
SUMMARY OF OBSERVATIONS

Instrument	Target	Aperture	Dataset ID	Observation Date	t_{exp} (ks)	
<i>HST</i> /STIS ^a	HE 0226–4110	$0.2'' \times 0.06''$	O6E107020,30	2002 Dec 26	6.0	
			O6E108010,20,30	2002 Dec 26	8.2	
			O6E109020,30	2002 Dec 27	6.0	
			O6E110010,20,30	2002 Dec 29	8.2	
			O6E111010,20	2002 Dec 31	5.1	
			O6E111030,40	2003 Jan 01	6.0	
			Total=39.6			
PG 0953+414	$0.2'' \times 0.2''$		O4X001010,20	1998 Dec 11	13.7	
			O4X002010	1998 Dec 04	10.7	
			Total=24.4			
<i>FUSE</i> ^b	HE 0226–4110	$30'' \times 30''$	P2071301 (v2.1.6)	2000 Dec 12	11.0	
			P1019101 (v2.1.6)	2001 Oct 03	50.3	
			P1019102 (v2.4.0)	2002 Nov 15	14.5	
			P1019103 (v2.4.0)	2002 Nov 16	18.9	
			P1019104 (v2.4.0)	2002 Nov 17	18.1	
			D0270101 (v2.4.0)	2003 Sep 01	23.9	
			D0270102 (v2.4.0)	2003 Sep 03	39.9	
			D0270103 (v2.4.0)	2003 Oct 31	16.7	
			Total=193.3			
			PG 0953+414	$30'' \times 30''$		P1012202 (v2.4.0)
	P1012201 (v2.1.6)	2000 May 04				36.5
	Total=75.4					

^aAll STIS observations were taken with the E140M grating, providing 6.7 km s^{-1} resolution (FWHM). The unbinned pixel size is between 3.0 and 3.2 km s^{-1} (varying with wavelength).

^bThe *FUSE* resolution is $\approx 20 \text{ km s}^{-1}$ (FWHM) in the LiF channels, and $\approx 25 \text{ km s}^{-1}$ in the SiC channels. Unbinned pixels are 2.0 km s^{-1} wide. We list the CALFUSE pipeline version used in parentheses after the Dataset ID. The difference between v2.1.6 and v2.4.0 is negligible.

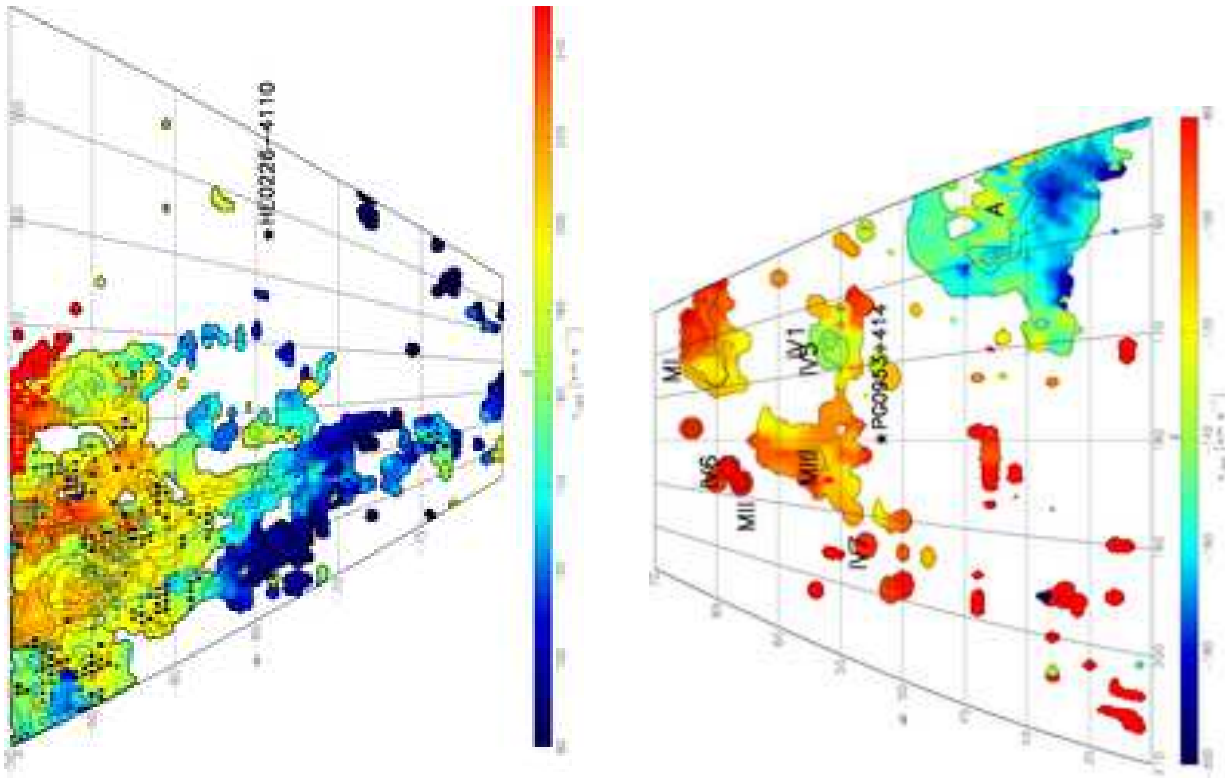


FIG. 1.— Maps in Galactic coordinates (l, b) of the HVC velocity field in the regions around HE 0226–4110 and PG 0953+414, based on the H I 21-cm data of Hulsbosch & Wakker (1988) and Morras et al. (2000). Colors show v_{LSR} , and contours are at brightness temperature levels of 0.05, 0.5, and 1 K, corresponding to column densities of about 2, 20, and $40 \times 10^{18} \text{ cm}^{-2}$. Individual cloud cores are labeled in the PG 0953+414 panel.

TABLE 3
MEASUREMENTS OF HVC ABSORPTION TOWARD HE 0226–4110

Line	S/N ^a	HV1, 80 to 125 km s ⁻¹				HV2, 125 to 160 km s ⁻¹				HV3, 160 to 185 km s ⁻¹				HV4, 185 to 200 km s ⁻¹		
		\bar{v}^b	b^c	W_λ^d	$\log N_a^e$	\bar{v}^b	b^c	W_λ^d	$\log N_a^e$	\bar{v}^b	b^c	W_λ^d	$\log N_a^e$	\bar{v}^b	b^c	W_λ^d
H I λ 920.963	10	92±5	25±2	136±07±08	16.29 ^{+0.02+0.04} _{-0.02-0.04}	147±6	14±2	88±05±10	16.16 ^{+0.06+0.18} _{-0.07-0.31}	172±5	12±1	85±03±17	16.20 ^{+0.08+0.30} _{-0.11-0.30}	201±6	19±3	107±07
H I λ 919.351	9	f	f	146±7	15±2	79±05±06	16.21 ^{+0.05+0.05} _{-0.07-0.06}	173±6	12±1	72±04±11	16.26 ^{+0.07+0.07} _{-0.07-0.08}	203±6	19±2	110±07
H I λ 918.129	8	90±7	27±2	97±12±07	16.30 ^{+0.07+0.03} _{-0.08+0.06}	147±7	15±2	64±07±09	16.15 ^{+0.07+0.08} _{-0.08-0.08}	174±5	11±1	70±04±11	16.36 ^{+0.06+0.07} _{-0.08-0.10}	199±6	17±2	95±07
H I λ 917.181	8	90±14	29±3	48±23±07	16.02 ^{+0.17+0.07} _{-0.12+0.06}	145±6	15±2	70±08±07	16.32 ^{+0.06+0.04} _{-0.07-0.34}	173±5	10±1	68±05±11	16.44 ^{+0.05+0.09} _{-0.05-0.11}	197±7	15±3	62±12
C II λ 1334.532	9	104±7	16±3	52±06±04	13.52 ^{+0.05+0.02} _{-0.07-0.03}	145±3	13±1	91±05±03	13.90 ^{+0.07+0.01} _{-0.09-0.01}	175±9	10±3	56±04±03	13.63 ^{+0.04+0.05} _{-0.05-0.07}	198±5	14±3	101±06
C II λ 1036.337	22	107±7	18±4	33±04±07	13.50 ^{+0.05+0.06} _{-0.06-0.06}	146±6	15±2	52±03±07	13.77 ^{+0.03+0.06} _{-0.03-0.07}	f	f	
C III λ 977.020	8	105±8	19±6	83±06±09	13.28 ^{+0.03+0.05} _{-0.02-0.05}	146±6	12±6	93±04±13	13.59 ^{+0.04+0.70} _{-0.03-0.23}	174±6	10±6	89±03±17	13.92 ^{+0.03+1.00} _{-0.03-0.23}	197±6	15±6	123±03
C IV λ 1550.770	9	<45	<13.35	150±7	14±5	37±10±11	13.36 ^{+0.14+0.05} _{-0.20-0.05}	167±7	8±2	25±09±08	13.20 ^{+0.13+0.04} _{-0.18-0.05}	213±6	13±4	35±12
N I λ 1200.710	6	<43	<13.88	<21	<13.58	<26	<13.66	<3
N II λ 1083.994	6	<55	<13.68	<42	<13.57	<33	<13.46	<4
N V λ 1238.821	10	<44	<13.32	<21	<13.00	<20	<12.97	<4
O I λ 1302.169	12	<23	<13.48	<29	<13.58	<16	<13.33	<1
O VI λ 1031.926	22	90±3	33±2	21±04±03	13.25 ^{+0.10+0.07} _{-0.11-0.07}	145±6	15±1	26±03±03	13.36 ^{+0.06+0.08} _{-0.06-0.09}	173±6	11±1	23±03±06	13.34 ^{+0.05+0.06} _{-0.06-0.07}	201±7	15±2	22±04
O VI λ 1037.617	24	<20	<13.50	f	f	f	f	
Si II λ 1260.422	9	102±7	18±3	47±08±04	12.58 ^{+0.10+0.02} _{-0.12-0.01}	145±3	12±2	62±06±04	12.81 ^{+0.07+0.02} _{-0.08-0.02}	174±8	11±2	42±05±03	12.58 ^{+0.07+0.04} _{-0.09-0.05}	199±6	15±3	51±07
Si II λ 1193.290	6	101±9	21±6	27±12±04	12.70 ^{+0.20+0.03} _{-0.37-0.03}	145±4	12±3	34±10±03	12.78 ^{+0.15+0.02} _{-0.23-0.01}	<42	<12.76	205±5	15±5	25±12
Si II λ 1190.416	6	105±6	15±4	32±13±03	13.05 ^{+0.19+0.03} _{-0.35-0.03}	138±7	10±3	22±11±09	12.89 ^{+0.18+0.04} _{-0.29-0.04}	176±6	8±3	29±09±09	12.99 ^{+0.13+0.02} _{-0.20-0.03}	<6
Si II λ 1526.710	10	<17	<12.88	<42	<13.27	<14	<12.80	206±5	18±4	24±08
Si III λ 1206.500	6	88±7	9±4	25±08±08	12.22 ^{+0.16+0.02} _{-0.26-0.02}	146±5	14±2	79±07±06	12.76 ^{+0.07+0.02} _{-0.08-0.02}	173±8	10±1	63±06±07	12.67 ^{+0.08+0.04} _{-0.09-0.03}	202±5	13±3	100±08
Si IV λ 1393.755	10	<34	<12.57	<30	<12.52	<21	<12.36	202±3	10±5	37±07
Si IV λ 1402.770	12	<21	<12.67	<23	<12.72	<37	<12.92	200±5	18±2	38±09
P II λ 1152.818	15	<34	<13.09	<25	<12.95	<23	<12.92	<1
S II λ 1259.519	10	<34	<14.17	<32	<14.14	f	f	f
S II λ 1253.811	11	<26	<14.23	<25	<14.22	<20	<14.12	<2
S III λ 1012.495	20	<20	<13.71	<12	<13.48	<15	<13.58	<1
Ar I λ 1048.220	26	<16	<12.81	<12	<12.68	<18	<12.86	<1
Fe II λ 1144.938	16	<17	<13.14	145±2	8±3	11±4±5	13.01 ^{+0.10+0.14} _{-0.12-0.21}	<10	<12.88	<1
Fe II λ 1608.451	6	<91	<13.81	<45	<13.50	<41	<13.46	<7
Fe III λ 1122.524	17	<17	<13.27	f	f	f	f	f

^aSignal-to-noise per resolution element in the continuum next to the line.

$$b_v = \frac{\int_{v_-}^{v_+} v \tau_a(v) dv / \int_{v_-}^{v_+} \tau_a(v) dv}{\int_{v_-}^{v_+} v \tau_a(v) dv / \int_{v_-}^{v_+} \tau_a(v) dv} \text{ (km s}^{-1}\text{)}.$$

$$c_b = \sqrt{2 \int_{v_-}^{v_+} (v - \bar{v})^2 \tau_a(v) dv / \int_{v_-}^{v_+} \tau_a(v) dv}. \text{ (km s}^{-1}\text{)}.$$

^dEquivalent width measured between quoted velocity limits (mÅ), with statistical and systematic errors.

^eApparent column density between quoted velocity limits, with statistical and systematic errors, or, for non-detections, 3σ limit set on the column density using 3σ equivalent width limit and linear COG. N_a is in cm⁻².

^fNo measurement or upper limit possible, because of blending with other lines. We list here the contaminated line, contaminated components, blending line and velocity: H I λ 919.351, HV1, O I λ 919.658 at $v \approx 0$; C II λ 1036.337, HV3-4, C II* λ 1037.0 HV1-4, N I λ 1200.223 at $v \approx 0$; N I λ 1200.223, HV1-4, N I λ 1200.710 at $v \approx 0$; O VI λ 1037.617, HV2-4, H₂ λ 1038.156 at $v \approx 0$; S II λ 1259.519, HV3-4, Si II λ 1260.422 at $v \approx 0$; Fe III λ 1122.524, HV2-4, IGM Ly ζ at $z = 0.20701$.

TABLE 4
MEASUREMENTS OF HVC ABSORPTION TOWARD PG 0953+414

Line	S/N ^a	HV1, -165 to -125 km s ⁻¹				HV2, 80 to 160 km s ⁻¹ g			
		\bar{v}^b	b^c	W_λ^d	$\log N_a^e$	\bar{v}^b	b^c	W_λ^d	$\log N_a^e$
H I λ 920.963	9	-153±8	19±4	89±07±10	16.09 ^{+0.02+0.05} _{-0.03-0.07}	114±6	23±3	125±09±08	16.26 ^{+0.04+0.01} _{-0.06-0.02}
H I λ 919.351	9	-149±6	16±4	74±07±10	16.13 ^{+0.04+0.07} _{-0.03-0.07}	f	
H I λ 918.129	9	-138±8	16±2	77±08±10	16.24 ^{+0.03+0.07} _{-0.03-0.08}	109±7	14±8	73±12±08	16.20 ^{+0.08+0.02} _{-0.10-0.02}
H I λ 917.181	9	f	f	118±10	24±3	84±11±09	16.32 ^{+0.08+0.03} _{-0.09-0.02}
C II λ 1334.532	12	-147±6	12±4	54±05±02	13.57 ^{+0.05+0.02} _{-0.05-0.02}	116±6	15±7	49±09±03	13.48 ^{+0.07+0.01} _{-0.08-0.01}
C II λ 1036.337	12	<38	<13.53	<46	<13.59
C III λ 977.020	13	f	f	127±7	40±5	25±14±16	13.77 ^{+0.02+0.04} _{-0.02-0.04}
C IV λ 1548.195	9	<38	<12.97	153±6	23±4	35±13±01	12.99 ^{+0.13+0.01} _{-0.20-0.01}
C IV λ 1550.770	8	<47	<13.36	<38	<13.27
N I λ 1199.550	7	<45	<13.42	f	f
N I λ 1200.710	7	f	f	<86	<14.19
N II λ 1083.994	6	<58	<13.71	<101	<13.95
N V λ 1238.821	9	<22	<13.01	<45	<13.32
O I λ 1302.169	12	<19	<13.39	113±10	33±6	23±08±02	13.53 ^{+0.12+0.03} _{-0.17-0.03}
O VI λ 1031.926	14	<39	<13.49	110±11	37±5	60±07±10	13.74 ^{+0.05+0.06} _{-0.05-0.06}
Si II λ 1260.422	12	-147±7	14±4	44±04±02	12.57 ^{+0.05+0.01} _{-0.05-0.01}	<43	<12.45
Si II λ 1193.290	6	<38	<12.71	<63	<12.93
Si II λ 1190.416	6	<61	<13.22	<44	<13.07
Si II λ 1526.710	14	<29	<13.10	<24	<13.02
Si III λ 1206.500	9	-144±2	12±4	55±07±08	12.55 ^{+0.03+0.06} _{-0.02-0.07}	128±8	42±4	30±14±11	12.90 ^{+0.05+0.01} _{-0.05-0.01}
Si IV λ 1393.755	11	-144±7	15±3	20±07±03	12.39 ^{+0.14+0.03} _{-0.19-0.02}	150±6	14±6	18±08±02	12.34 ^{+0.16+0.02} _{-0.24-0.01}
Si IV λ 1402.770	9	<25	<12.74	<36	<12.90
P II λ 1152.818	17	<27	<12.99	<42	<13.18
S II λ 1259.519	12	<12	<13.74	<03	<13.52
S III λ 1012.495	16	<43	<14.05	f	f
Ar I λ 1048.220	18	<26	<13.02	<26	<13.02
Fe II λ 1144.938	18	<35	<13.44	<34	<13.13
Fe III λ 1122.524	18	f	f	<47	<13.72

^aSignal-to-noise per resolution element in the continuum next to the line.

^b $\bar{v} = \int_{v_-}^{v_+} v \tau_a(v) dv / \int_{v_-}^{v_+} \tau_a(v) dv$ (km s⁻¹).

^c $b = \sqrt{2 \int_{v_-}^{v_+} (v - \bar{v})^2 \tau_a(v) dv / \int_{v_-}^{v_+} \tau_a(v) dv}$. (km s⁻¹).

^dEquivalent width measured between quoted velocity limits (mÅ), with statistical and systematic errors.

^eApparent column density between quoted velocity limits, with statistical and systematic errors, or, for non-detections, 3 σ limit set on the column density using 3 σ equivalent width limit and linear COG. N_a is in cm⁻².

^fNo measurement or upper limit possible, because of blending. We list here the contaminated line, contaminated components, blending line and velocity: H I λ 919.351, HV2, O I λ 919.658 at $v \approx 0$; H I λ 917.181, HV1, edge of detector; C III λ 977.020, HV1, H₂ λ 976.552 at $v \approx 0$; N I λ 1199.550, HV2, N I λ 1200.223 at $v \approx 0$; N I λ 1200.223, HV1, N I λ 1199.550 at $v \approx 0$; N I λ 1200.223, HV2, N I λ 1200.710 at $v \approx 0$; N I λ 1200.710, HV1, N I λ 1200.223 at $v \approx 0$; O VI λ 1037.617, HV1, H₂ λ 1037.146 at $v \approx 0$; O VI λ 1037.617, HV2, H₂ λ 1038.156 at $v \approx 0$; S III λ 1012.495, HV2, H₂ λ 1012.822 at $v \approx 0$; Fe III λ 1122.524, HV1, Fe II λ 1121.975 at $v \approx 0$.

^gMeasurements of C III, Si III, S III, Fe III, and O VI in HV2 are made over the extended velocity range 80 to 200 km s⁻¹; measurements of C IV, N V, and Si IV are made over 125 to 200 km s⁻¹.

TABLE 5
SUMMARY OF HVC COLUMN DENSITY MEASUREMENTS

Sight Line	Comp.	H I	C II	C III	C IV	Si II	Si III	Si IV	O VI
HE 0226-4110	HV1	16.29±0.05	13.53 ^{+0.05} _{-0.07}	13.28 ^{+0.06} _{-0.05}	<13.35	12.65 ^{+0.10} _{-0.10}	12.22 ^{+0.16} _{-0.26}	<12.57	13.25 ^{+0.13} _{-0.12}
	HV2	16.21±0.10	13.90 ^{+0.34} _{-0.09}	13.59 ^{+0.70} _{-0.16}	13.36 ^{+0.15} _{-0.21}	12.81 ^{+0.25} _{-0.08}	12.76 ^{+0.07} _{-0.08}	<12.52	13.36 ^{+0.10} _{-0.11}
	HV3	16.74±0.20 ^a	13.63 ^{+0.06} _{-0.07}	13.92 ^{+1.00} _{-0.23}	13.20 ^{+0.14} _{-0.19}	12.70 ^{+0.07} _{-0.07}	12.67 ^{+0.09} _{-0.09}	<12.36	13.34 ^{+0.08} _{-0.09}
	HV4	16.34±0.10	13.92 ^{+0.25} _{-0.05}	13.90 ^{+1.00} _{-0.05}	13.31 ^{+0.17} _{-0.28}	12.71 ^{+0.08} _{-0.08}	12.89 ^{+0.28} _{-0.07}	12.85 ^{+0.15} _{-0.15}	13.29 ^{+0.09} _{-0.11}
PG 0953+414	HV1	16.15±0.15	13.57 ^{+0.05} _{-0.05}	...	<12.97	12.57 ^{+0.05} _{-0.05}	12.55 ^{+0.07} _{-0.07}	12.39 ^{+0.14} _{-0.19}	<13.49
	HV2	16.26±0.15	13.48 ^{+0.07} _{-0.08}	13.77 ^{+0.25} _{-0.04}	12.99 ^{+0.13} _{-0.20}	<12.45	12.90 ^{+0.05} _{-0.05}	12.34 ^{+0.16} _{-0.24}	13.74 ^{+0.08} _{-0.08}

NOTE. — All measurements in this table are the logarithm of the ionic column density in cm⁻². Errors are $\pm 1\sigma$; upper/lower limits are 3 σ . For cases where absorption column densities are measured in more than one line (particularly Si II), we considered the dispersion of individual measurements and their errors to determine the final value listed.

^aComponent saturated, even in weakest Lyman lines; column density estimated using AOD correction method for saturated lines (Savage & Sembach 1991).

TABLE 6
FLUX OF IONIZING RADIATION NEAR THE GALAXY

Sight Line	b ($^{\circ}$)	Model ^a	Distance (kpc)	$\log \Phi_{<912}^b$ (Φ in $\text{cm}^{-2} \text{s}^{-1}$)	$\log \Phi_{>912}^b$ (Φ in $\text{cm}^{-2} \text{s}^{-1}$)
HE 0226–4110	–66	MW	10	5.0	7.0
			50	4.5	6.5
			100	3.8	5.8
PG 0953+414	+52	EGB	...	4.0	4.8
		MW	10	5.5	7.5
			50	4.7	6.6
			100	3.8	6.2
		EGB	...	4.0	4.8

^aMW = escaping Milky Way radiation (see §6.2); EGB = extragalactic background radiation (Haardt & Madau 1996).

^bTotal ionizing flux impinging on the clouds at hydrogen-ionizing (hard; $\lambda < 912 \text{ \AA}$) and non-hydrogen-ionizing (soft; $2460 \text{ \AA} > \lambda > 912 \text{ \AA}$) wavelengths. We assume $F_{\nu} = 4\pi J_{\nu}$ when computing Φ for the EGB (see §6.1).

TABLE 7
RESULTS OF HVC PHOTOIONIZATION MODELING

Sight Line	Comp.	\bar{v} (km s^{-1})	Model	Dist. (kpc)	$\log U^a$	$[Z/H]^b$	$\log n_{\text{H}}^c$ (n_{H} in cm^{-3})	l^d (pc)	P/k^e ($\text{cm}^{-3} \text{K}$)	$f(\text{H II})^f$	$I(\text{H}\alpha)^g$ (mR)			
HE 0226–4110	HVC1	99	MW+EGB	10	–3.75	–0.6	–1.7	11	470	0.98	2.2			
				50	–3.70	–0.6	–2.1	39	170	0.98	0.8			
				100	–3.80	–0.6	–2.4	56	79	0.97	0.3			
			EGB	...	–3.80	–0.5	–2.6	86	51	0.97	0.2			
				HVC2	148	MW+EGB	10	–3.55	–0.4	–1.9	23	290	0.98	1.9
							50	–3.55	–0.4	–2.3	57	110	0.98	0.7
	100	–3.55	–0.3				–2.7	150	47	0.98	0.3			
	EGB	...	–3.55	–0.3	–2.9	230	30	0.98	0.2					
		HVC3	175	MW+EGB	10	–3.75	–0.9	–1.7	37	550	0.98	6.3		
					50	–3.70	–0.9	–2.1	120	190	0.98	2.3		
	100				–3.70	–0.9	–2.5	290	78	0.98	0.9			
	EGB	...	–3.70	–0.9	–2.7	440	50	0.98	0.5					
HVC4		193	MW+EGB	10	–3.50	–0.6	–1.9	38	240	0.98	2.6			
				50	–3.50	–0.6	–2.3	98	95	0.98	1.0			
	100			–3.50	–0.5	–2.7	240	39	0.98	0.4				
EGB	...	–3.45	–0.4	–3.0	500	25	0.99	0.2						
	HVC1	–150	MW+EGB	10	–3.70	–0.6	–1.2	3	1180	0.98	5.2			
				50	–3.65	–0.6	–2.0	24	200	0.98	0.9			
100				–3.66	–0.6	–2.5	81	59	0.98	0.3				
EGB			...	–3.60	–0.5	–2.8	170	36	0.98	0.1				
			HVC2	–125	MW+EGB	10	–3.15	–0.9	–1.8	56	460	1.00	5.0	
						50	–3.15	–0.8	–2.5	310	86	1.00	0.9	
100	–3.11	–0.8				–3.1	1290	24	1.00	0.2				
EGB	...	–3.20	–0.7	–3.2	1270	18	0.99	0.1						

NOTE. — Our photoionization models are conducted by finding the values of the ionization parameter U and metallicity $[Z/H]$ that best reproduce the observed ionic column densities of H I, C II, C III, Si II, and Si III, for a given input radiation field at a given distance.

^aBest fit ionization parameter, ± 0.2 dex (95% c.l.).

^bBest fit metallicity, ± 0.2 dex (95% c.l.), or ± 0.3 dex for HE 0226–4110 HVC3 and HVC4, where saturation may affect the C III line.

^cTotal hydrogen density: $n_{\text{H}} = n_{\gamma}/U \text{ cm}^{-3}$, where n_{γ} is the density of ionizing photons in the radiation field.

^dCloud depth: $l = N_{\text{H}}/n_{\text{H}}$, where N_{H} is the total hydrogen column density returned by the model.

^eHVC pressure, $P/k = \sum_i n_i T$, summing over all elements and ionization states i and their associated electrons.

^fHydrogen ionization fraction.

^gPredicted intensity of H α emission: $I(\text{H}\alpha) = 2.75(T/10^4 \text{ K})^{0.924} n_{\text{e}}^2 l$ Rayleighs (R), where $1 \text{ R} = 10^6/4\pi \text{ photons cm}^{-2} \text{ s}^{-1} \text{ sr}^{-1}$.

TABLE 8
HIGH ION COLUMN DENSITY RATIOS IN HVCs^a

Sight Line	\bar{v} (km s ⁻¹)	$\frac{N(\text{H I})}{N(\text{O VI})}$	$\frac{N(\text{Si IV})}{N(\text{O VI})}$	$\frac{N(\text{C IV})}{N(\text{O VI})}$	$\frac{N(\text{N V})}{N(\text{O VI})}$	$\frac{N(\text{C IV})}{N(\text{Si IV})}$
HE 0226-4110	+ 99	1100 ⁺³⁰⁰ ₋₄₀₀	<0.12	<0.72	<0.80	...
	+148	710 ⁺²⁴⁰ ₋₂₃₀	<0.08	1.0 ± 0.5	<0.26	>10
	+175	2500 ⁺¹⁵⁰⁰ ₋₁₁₀₀	<0.05	0.7 ± 0.3	<0.23	>10
	+193	1100 ⁺⁴⁰⁰ ₋₃₀₀	0.36 ± 0.16	1.0 ± 0.5	<0.65	2.9 ± 1.8
PG 0953+414	-150	>600	>0.11	<2.6
	+124	330 ⁺¹⁵⁰ ₋₁₂₀	0.04 ± 0.02	0.18 ± 0.07	<0.19	4.5 ± 2.5
PG 1259+593 ^b	-110	(1.7 ± 0.3) × 10 ⁶	0.10 ± 0.02	0.35 ± 0.05	< 0.07	3.4 ± 0.4
Mrk 279 ^c	-140	(6.8 ± 1.6) × 10 ⁵	0.22 ± 0.07	0.89 ± 0.29	0.19 ± 0.07	4.0 ± 1.6
PKS 2155-304 ^d	-140	370 ⁺²⁵⁰ ₋₁₁₀	0.09 ± 0.02	0.51 ± 0.06	< 0.08	5.9 ± 1.1
	-170	47 ⁺⁶⁶ ₋₁₉	0.05 ± 0.02	1.1 ± 0.2	< 0.08	1.1 ± 0.2
Mrk 509 ^d	-240	< 2700	< 0.02	0.44 ± 0.07	< 0.07	> 25
	-300	< 2600	0.4 ± 0.2	1.7 ± 0.4	< 0.09	4.2 ± 2.0
PG 1116+215 ^e	+100	1350 ± 40	0.18 ± 0.06	1.12 ± 0.36	< 0.27	6.3 ± 1.3
	+184	7000 ⁺³⁰⁰⁰ ₋₂₀₀₀	0.12 ± 0.01	0.55 ± 0.07	< 0.05	4.5 ± 0.8
HVC average (detections only) ^f	0.17 ± 0.13	0.80 ± 0.42	0.19 ± 0.07	4.1 ± 1.6
Halo average ^g	0.20 ± 0.13	0.60 ± 0.47	0.12 ± 0.07	3.5 ± 1.1

^aRefer to Tables 3 and 4 for the velocity ranges and log N_a measurements for each component. Errors given are $\pm 1\sigma$; upper and lower limits are 3σ .

^bFrom Fox et al. (2004).

^cNew measurements of $N(\text{C IV})$ and $N(\text{Si IV})$ using archival spectra of Mrk 279. We measure $N(\text{C IV})=13.68^{+0.11+0.02}_{-0.15-0.02}$ and $N(\text{Si IV})=13.01^{+0.10+0.01}_{-0.13-0.01}$ in the range $v_{LSR}=-210$ to -115 km s⁻¹, where high-velocity O VI is detected.

^dFrom Collins et al. (2004).

^eFrom Ganguly et al. (2005).

^fMean value of detections, with quoted error representing sample standard deviation. Upper/lower limits are ignored.

^gFrom Zsargó et al. (2003). Errors represent sample standard deviation.

TABLE 9
ORIGIN MODELS FOR HIGHLY IONIZED HVC COMPONENTS

Origin	Ionization Source	Explains ^a	Explains ^a	Explains ^a	Ref.
		$\frac{N(\text{Si IV})}{N(\text{O VI})}$?	$\frac{N(\text{C IV})}{N(\text{O VI})}$?	$\frac{N(\text{N V})}{N(\text{O VI})}$?	
Galactic Fountain	Recombination of hot gas	0/8 (4/5)	1/12 (1/1)	0/1 (11/12)	(1)
HVC interface	Conductive Heating	2/8 (4/5)	11/12 (1/1)	1/1 (11/12)	(2)
	Turbulent Mixing	7/8 (2/5)	6/12 (0/1)	1/1 (6/12)	(3)
	Shock Heating	6/8 (5/5)	11/12 (1/1)	0/1 (12/12)	(4)

REFERENCES. — (1): Edgar & Chevalier (1986); (2): Borkowski et al. (1990); (3): Slavin et al. (1993); (4): Dopita & Sutherland (1996).

^aIn these columns we assess what fraction of highly ionized HVCs ratios (from this paper and the literature) can be reproduced (to within their $\pm 1\sigma$ errors) by the given model assuming solar abundances. The numbers in parentheses represent the fraction of upper/lower limits that are consistent with the model predictions. See Fox et al. (2004) for a tabulation of ionic ratio predictions in different models.

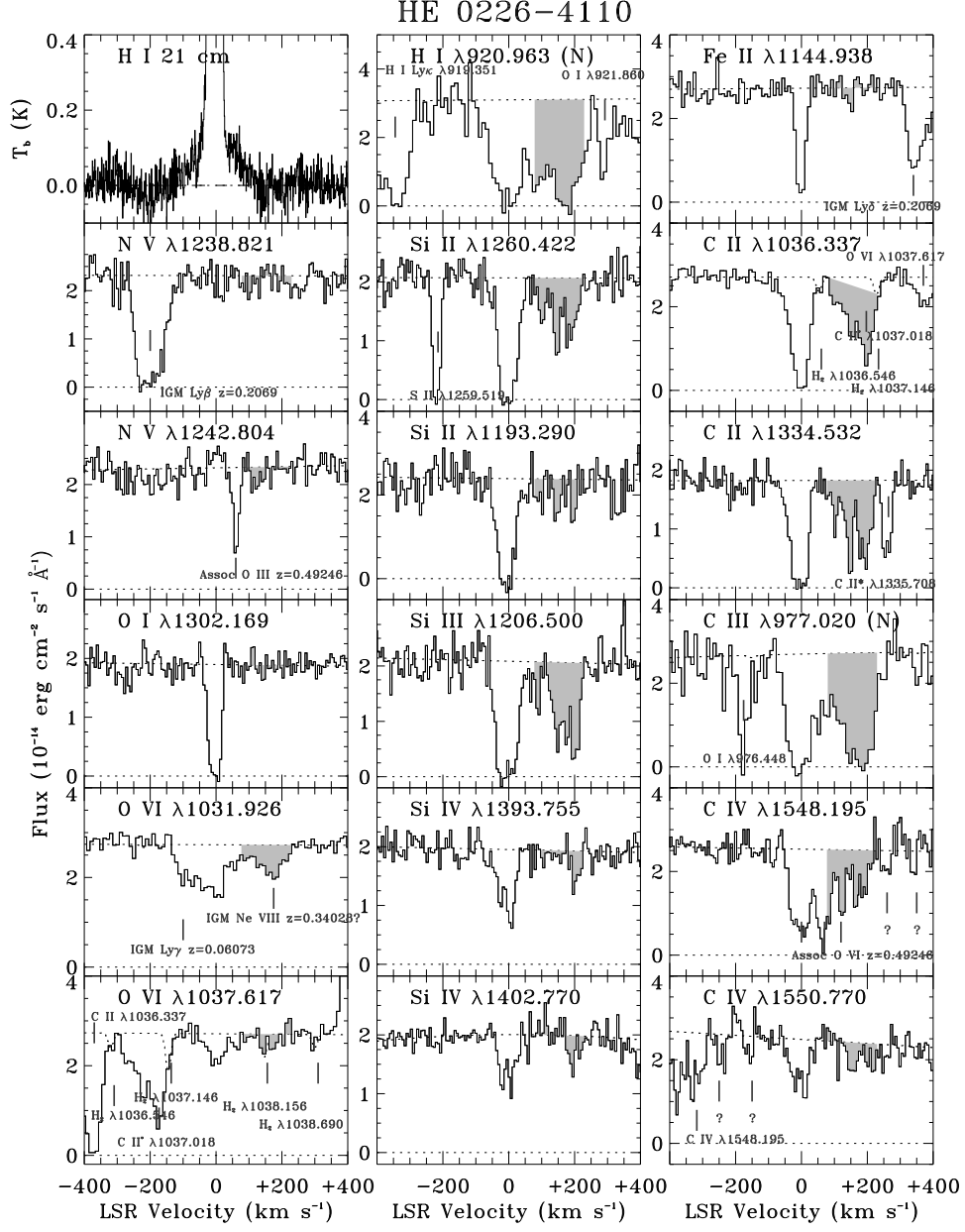


FIG. 2.— Absorption line profiles along the line of sight to HE 0226-4110. Flux is plotted against LSR velocity with the continuum and zero levels shown as dotted lines. The upper left panel shows the 21-cm emission line profile. Absorption in the HVCs is shaded, and blends are annotated at the expected line center of the offending feature. For O VI $\lambda 1037.617$ and C II $\lambda 1036.337$, the continuum includes a model of the H₂ lines. (N) indicates night-only data is displayed to reduce geocoronal airglow emission.

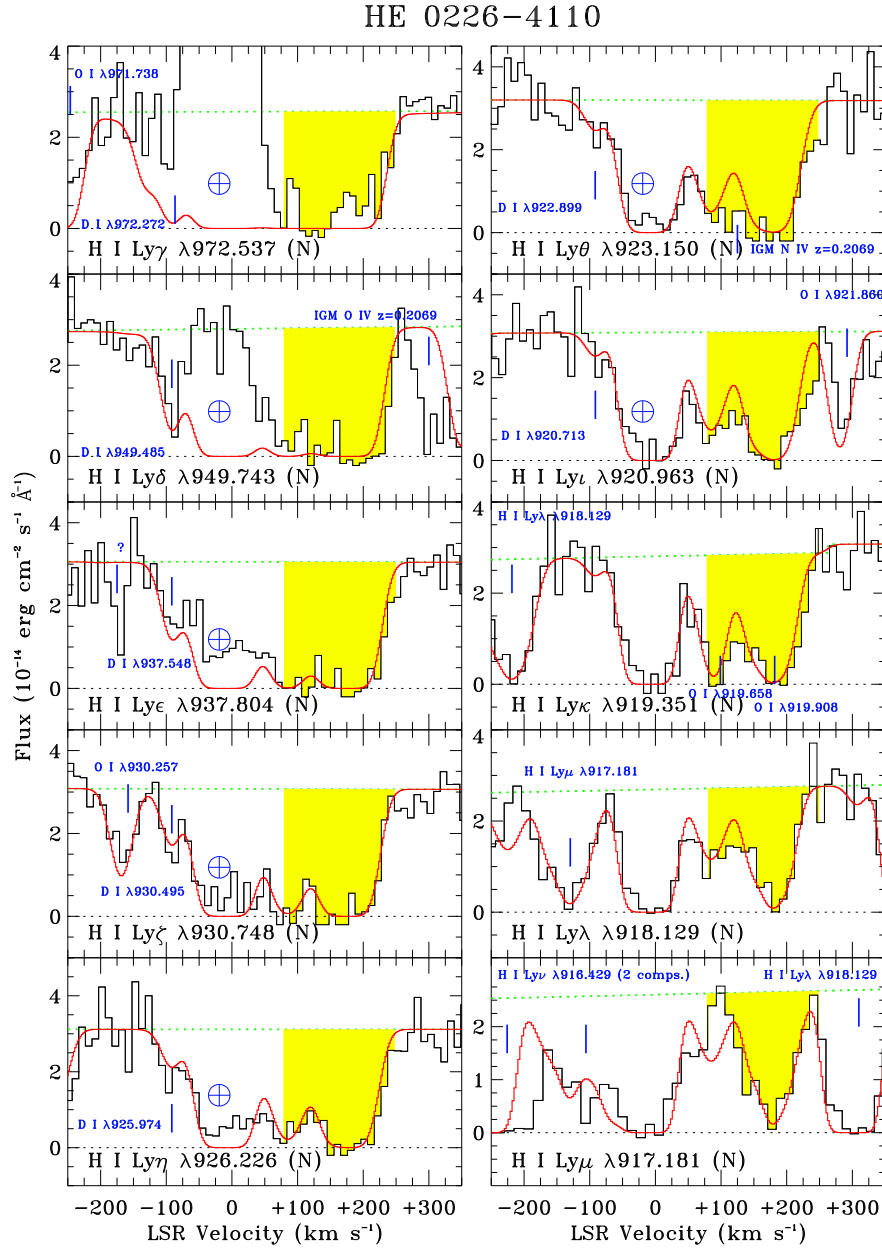


FIG. 3.— H I Lyman series absorption line profiles along the line of sight to HE 0226-4110. Dotted lines display the position of the continuum and the zero level. Geocoronal H I emission centered near 0 km s^{-1} is seen in the stronger lines and can be ignored. The red line shows a Voigt component model of the H I absorption, using the component velocities and column densities derived using the AOD method.

HE 0226-4110

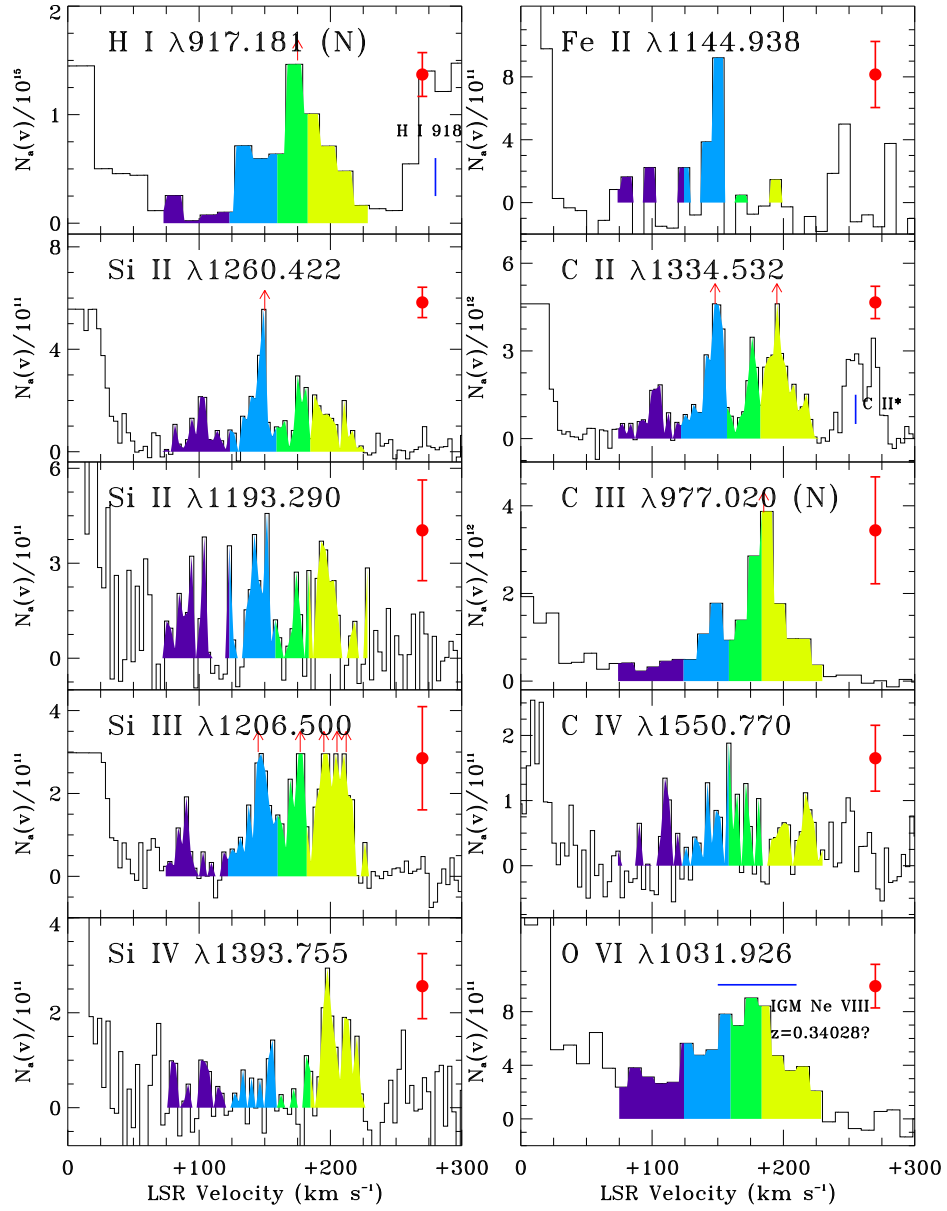


FIG. 4.— Comparison of apparent column density as a function of velocity for various species seen in the HVCs toward HE 0226-4110. The units on the y-axes are ions $\text{cm}^{-2} (\text{km s}^{-1})^{-1}$. Error bars showing the typical uncertainty on each data point are shown in the corner of each panel, and small red arrows indicate where the high-velocity absorption may be saturated. The color of the shading indicates the velocity range covered by each component.

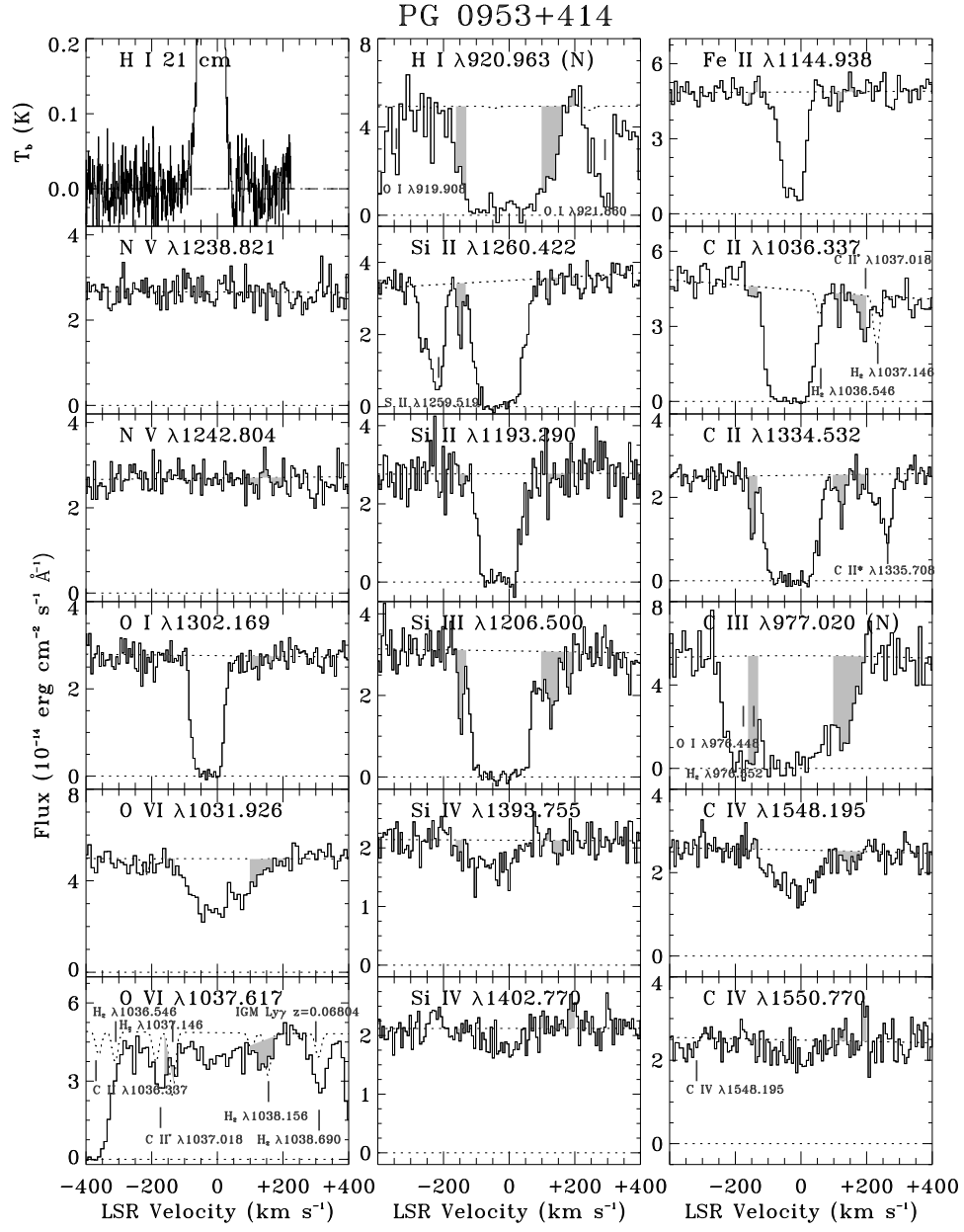


FIG. 5.— Same as Figure 2, except for PG 0953+414.

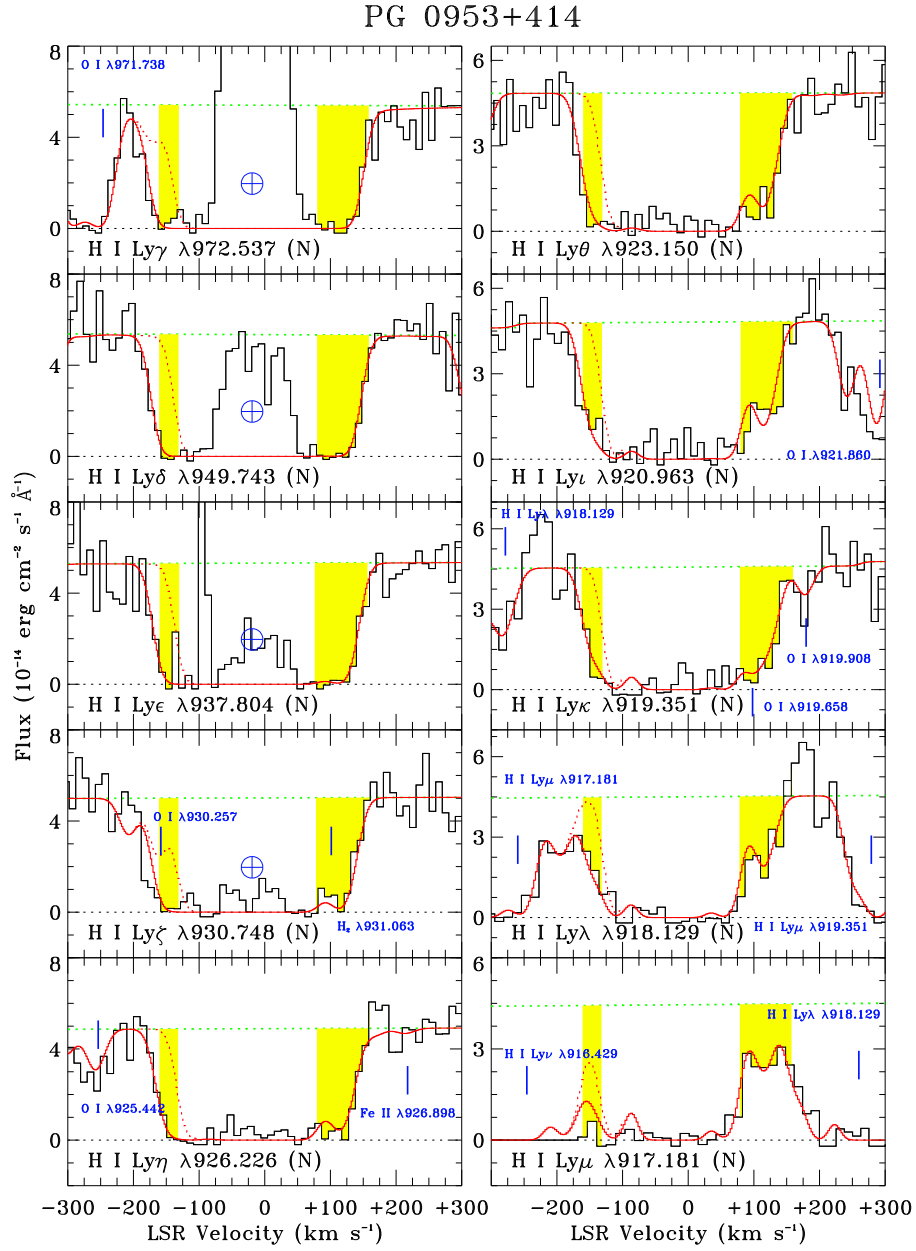


FIG. 6.— Same as Figure 3, except for PG 0953+414. The dotted red line shows the Voigt profile model without a component at -150 km s^{-1} ; this model clearly does not match the data, showing that H I exists and can be measured in the -150 km s^{-1} HVC.

PG 0953+414

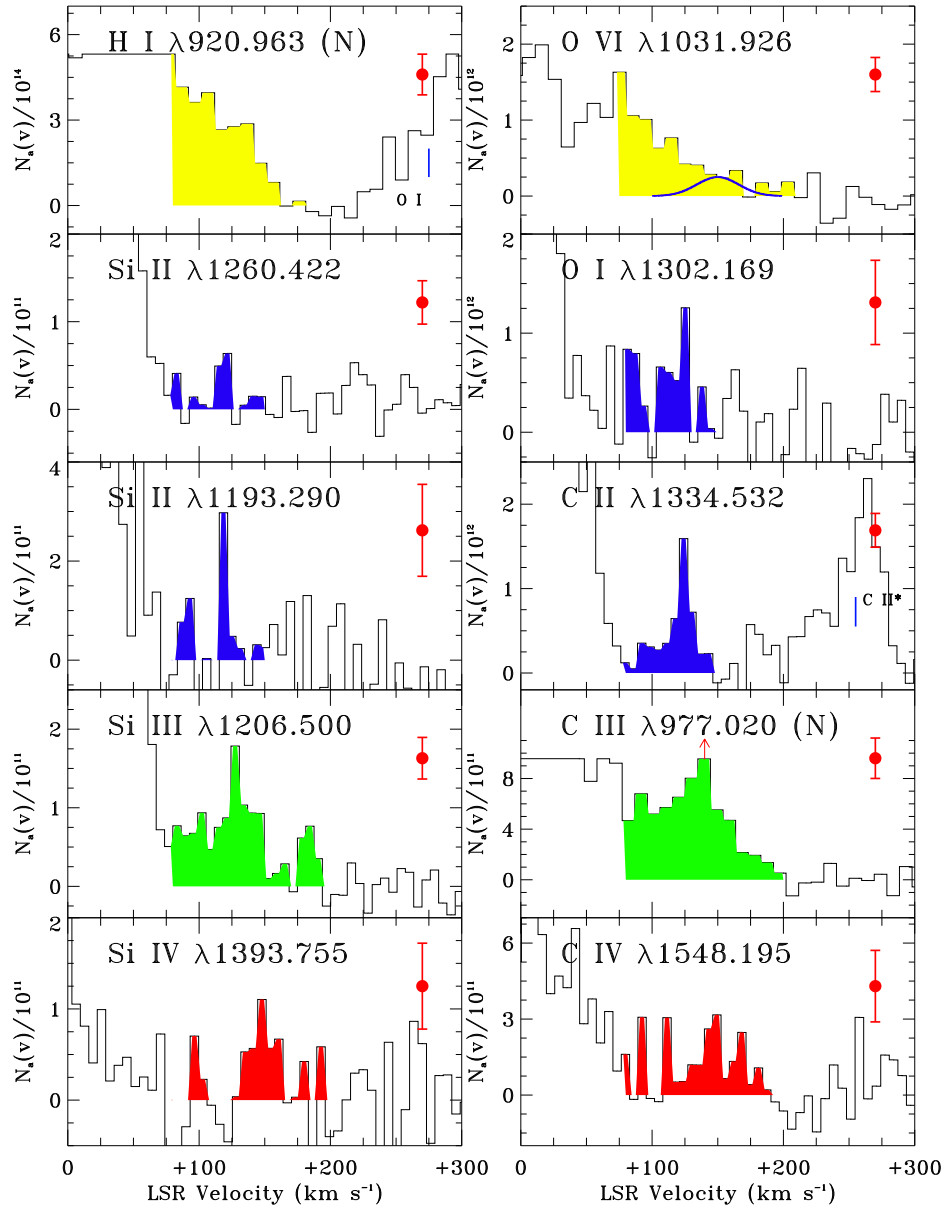


FIG. 7.— Same as Figure 4, except for PG 0953+414. The color scheme reflects the shape of the absorption profile: narrow (blue), broad (green), broad and offset (red), and wing-like (yellow). The thick solid line in the O VI panel shows the predicted contribution from a conductive interface with a velocity and width defined by the C IV and Si IV profiles, and with a typical C IV/O VI ratio.

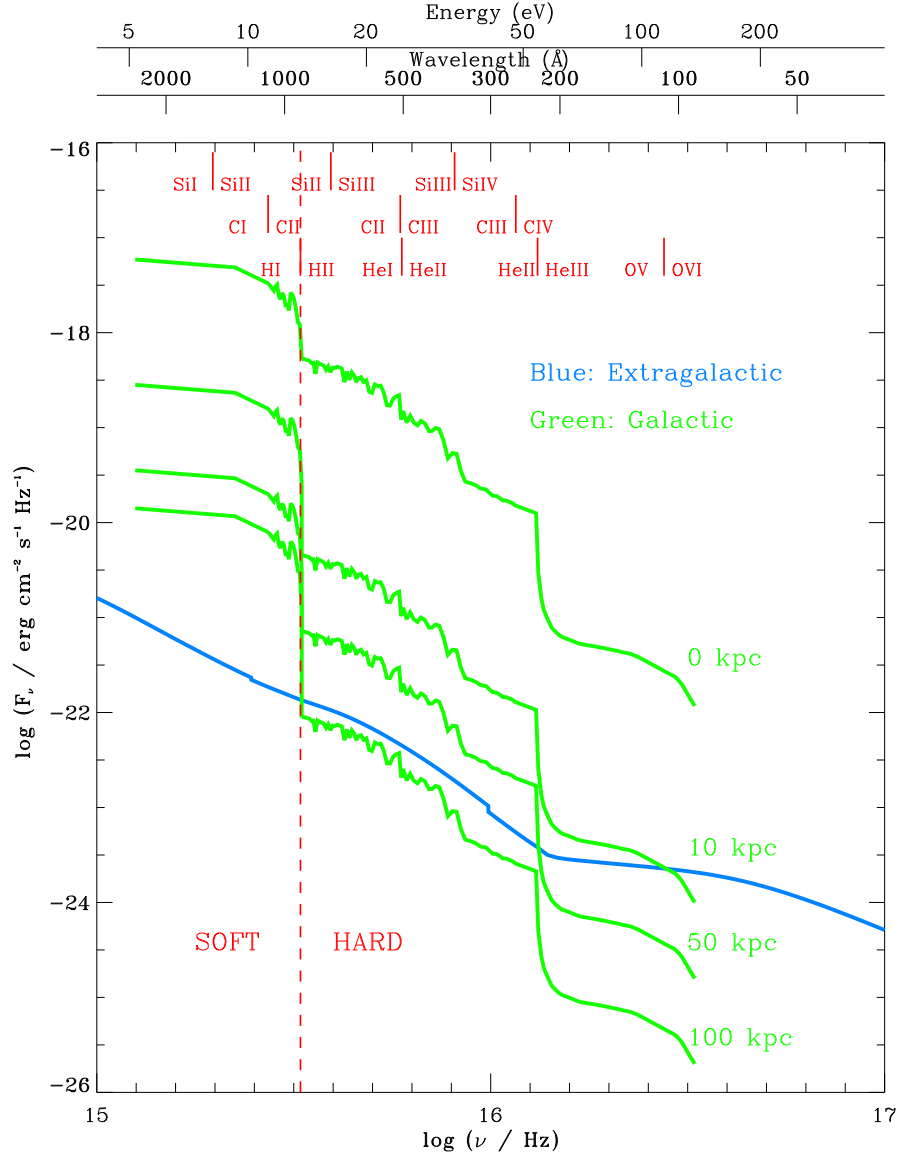


FIG. 8.— Radiation fields incident upon the HVCs in our CLOUDY calculations. The blue line shows the estimated extragalactic background flux, where $F_\nu = 4\pi J_\nu$ and J_ν is taken from Haardt & Madau (1996). The green line shows our new estimate of the flux of escaping Galactic radiation, at distances of 0, 10, 50, and 100 kpc along the PG 0953+414 sight line ($b = +52^\circ$). Note the substantial drop at 54 eV in the Galactic spectrum, caused by the He II edge in hot stars. Other ionization edges are marked at the top of the plot.

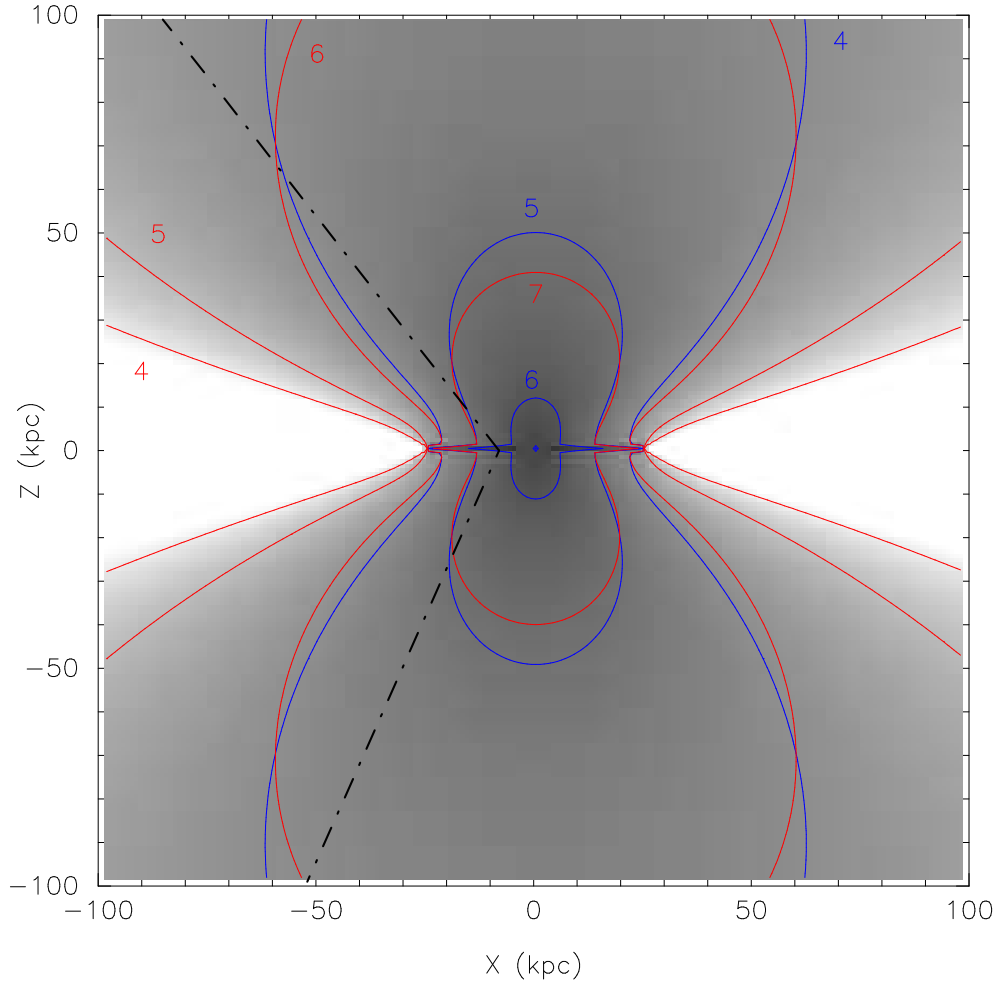


FIG. 9.— Contour plot showing the flux of Galactic radiation as a function of location relative to the Galactic disk in our new disk-halo model. The blue contours show the lines of constant hydrogen ionizing flux ($\Phi_{<912} = \int_0^{912} (F_\lambda/h\nu)d\lambda$), and the red contours show the lines of constant non-hydrogen ionizing flux ($\Phi_{>912} = \int_{912}^{2460} (F_\lambda/h\nu)d\lambda$). The numbers next to the contours are the logarithm of $\Phi_{<912}$ in units of $\text{cm}^{-2} \text{s}^{-1}$. The Galactic ionizing field dominates the extragalactic ionizing background inside the line defined by $\log \Phi = 4$. The dot-dashed lines show the sight lines of interest in this paper (PG 0953+414 above the plane and HE 0226–4110 below it). This map is used to scale the normalization of the Galactic disk ionizing spectrum shown in Figure 8 for use in our photoionization modeling.

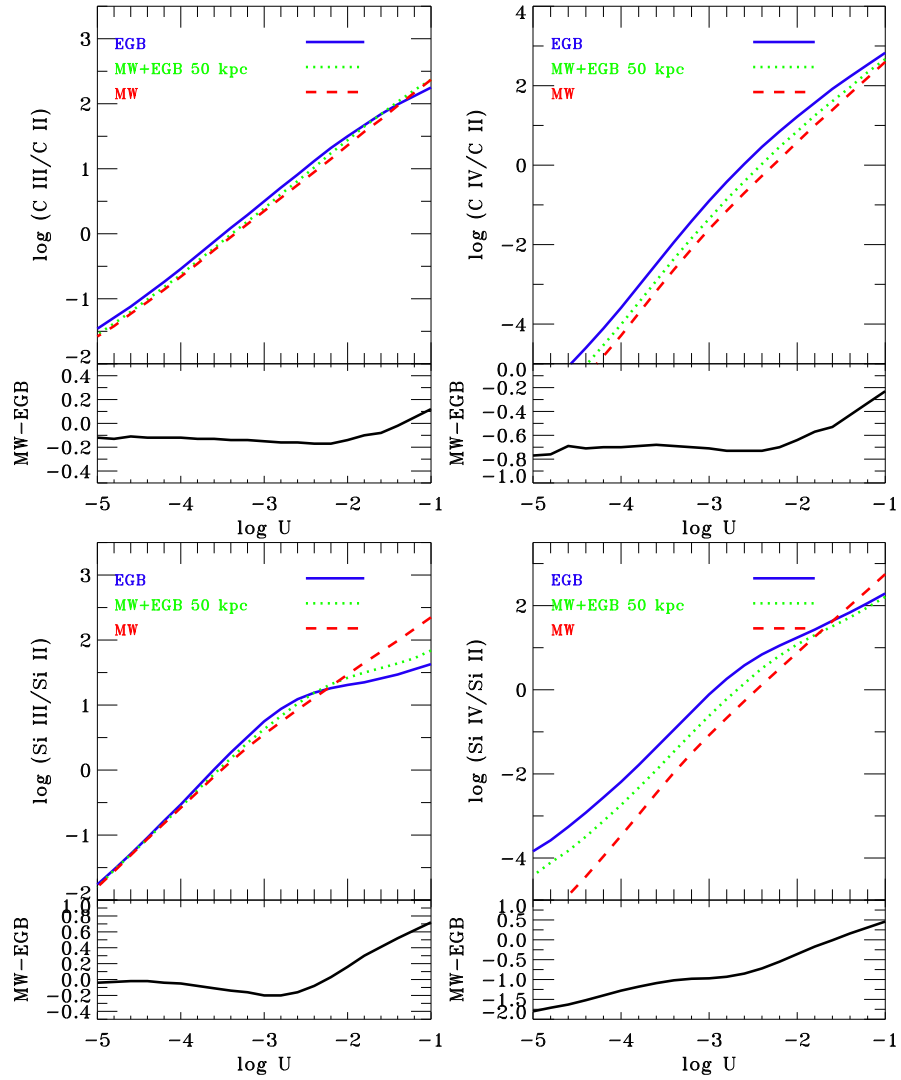


FIG. 10.— The behavior of various column density ratios of carbon and silicon as a function of ionization parameter, for HVCs immersed in three radiation fields: the EGB, the MW (any distance), and MW+EGB at 50 kpc toward HE 0226–4110. The logarithmic differences in the ionic ratios between the pure MW and pure EGB fields are shown in the panels labelled MW–EGB. Under the assumption of pure photoionization, these curves can be used to convert an observed ionic ratio to an implied ionization parameter, for a given radiation field.

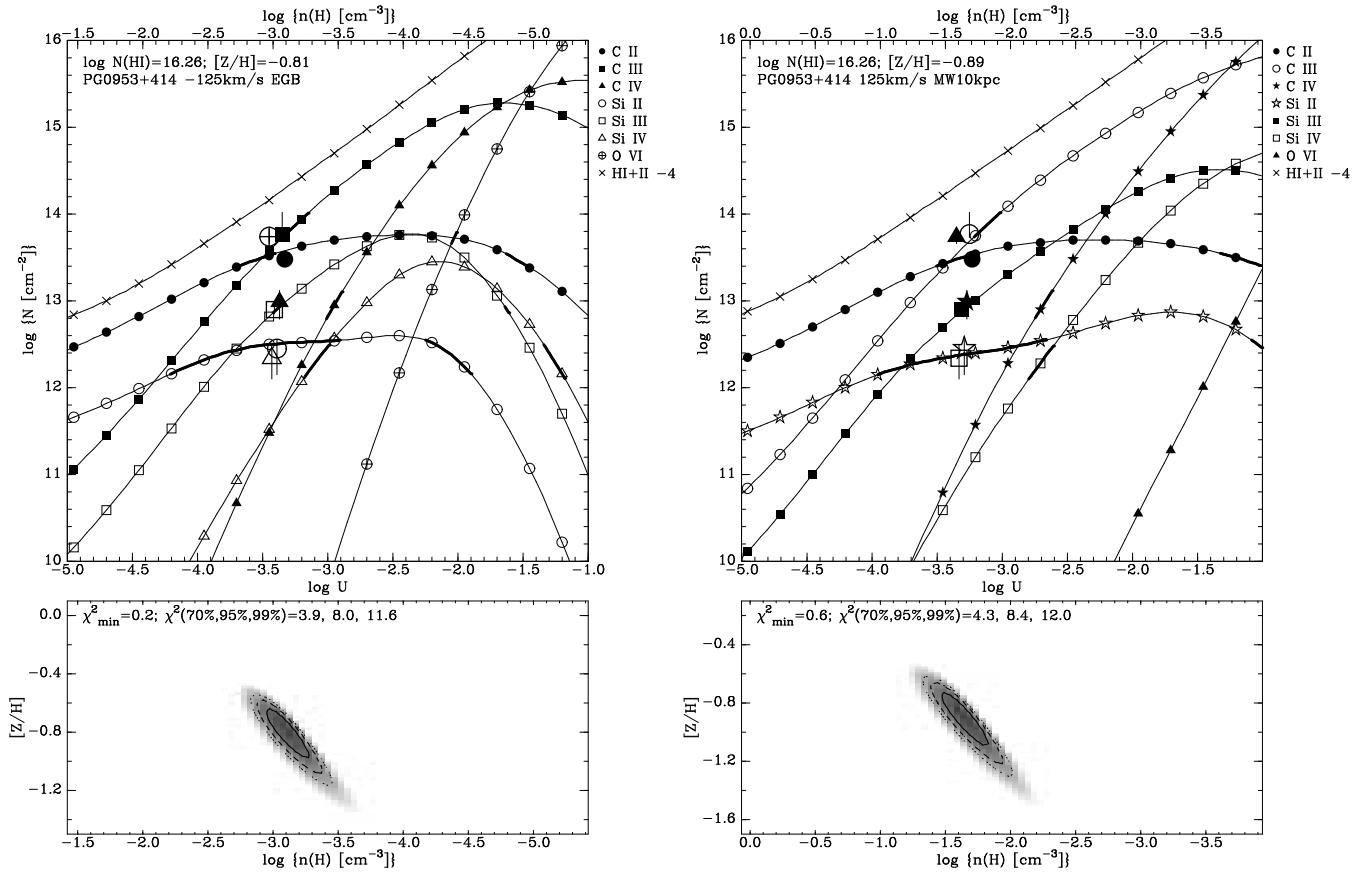


FIG. 11.— Example CLOUDY run showing the fits to observed column densities in HVC2 toward PG 0953+414, for two radiation fields: EGB (left) and MW+EGF at 10 kpc (right). For both radiation fields a good fit can be found to the C II, C III, Si II, and Si III data, but not the C IV, Si IV, or O VI. The best-fit $\log U$ and $[Z/\text{H}]$ and their errors are derived using a chi-squared minimization process, shown in the grayscale on the bottom panel. The contours show the regions of 70, 95, and 99% confidence. Results from models of this kind to all HVC components toward HE 0226–4110 and PG 0953+414 are given in Table 7.

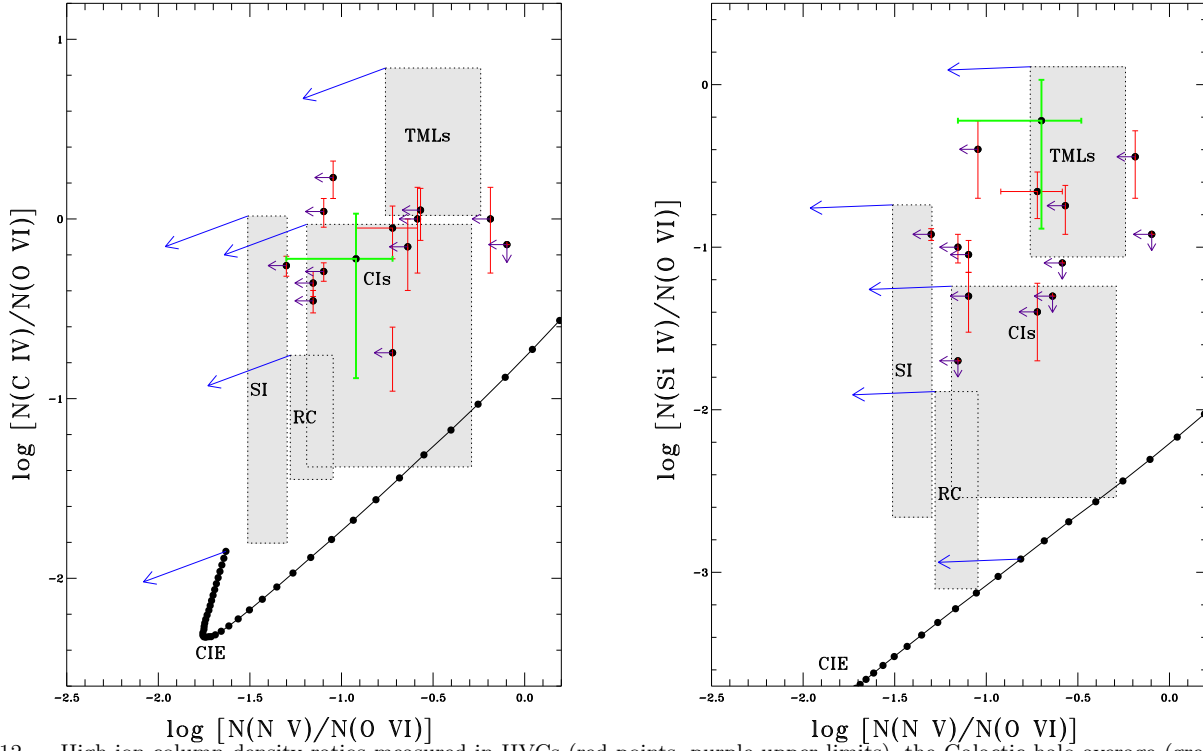


FIG. 12.— High-ion column density ratios measured in HVCs (red points, purple upper limits), the Galactic halo average (green point; Zsargó et al. 2003), and the predictions of various models (gray boxes). CIs = conductive interfaces; CIE = collisional ionization equilibrium; TMLs = turbulent mixing layers; RC = radiative cooling; SI = shock ionization. The blue arrows show the effect of correcting the model predictions with solar abundance ratios onto a Magellanic Stream set of abundances. See Fox et al. (2004) for a detailed explanation of the model parameters.